

Regulation of the mammalian-brain V-ATPase through ultraslow mode-switching

<https://doi.org/10.1038/s41586-022-05472-9>

Received: 13 January 2022

Accepted: 21 October 2022

Published online: 23 November 2022

 Check for updates

Eleftherios Kosmidis¹, Christopher G. Shuttle^{1,9}, Julia Preobraschenski^{2,3,4,9}, Marcelo Ganzella², Peter J. Johnson^{5,7}, Salome Veshaguri^{1,8}, Jesper Holmkvist¹, Mads P. Møller¹, Orestis Marantos¹, Frank Marcoline⁶, Michael Grabe⁶, Jesper L. Pedersen⁵, Reinhard Jahn² & Dimitrios Stamou^{1,✉}

Vacuolar-type adenosine triphosphatases (V-ATPases)^{1–3} are electrogenic rotary mechanoenzymes structurally related to F-type ATP synthases^{4,5}. They hydrolyse ATP to establish electrochemical proton gradients for a plethora of cellular processes^{1,3}. In neurons, the loading of all neurotransmitters into synaptic vesicles is energized by about one V-ATPase molecule per synaptic vesicle^{6,7}. To shed light on this bona fide single-molecule biological process, we investigated electrogenic proton-pumping by single mammalian-brain V-ATPases in single synaptic vesicles. Here we show that V-ATPases do not pump continuously in time, as suggested by observing the rotation of bacterial homologues⁸ and assuming strict ATP–proton coupling. Instead, they stochastically switch between three ultralong-lived modes: proton-pumping, inactive and proton-leaky. Notably, direct observation of pumping revealed that physiologically relevant concentrations of ATP do not regulate the intrinsic pumping rate. ATP regulates V-ATPase activity through the switching probability of the proton-pumping mode. By contrast, electrochemical proton gradients regulate the pumping rate and the switching of the pumping and inactive modes. A direct consequence of mode-switching is all-or-none stochastic fluctuations in the electrochemical gradient of synaptic vesicles that would be expected to introduce stochasticity in proton-driven secondary active loading of neurotransmitters and may thus have important implications for neurotransmission. This work reveals and emphasizes the mechanistic and biological importance of ultraslow mode-switching.

V-ATPases are a ubiquitous family of electrogenic ATP-driven rotary mechanoenzymes structurally related to F-type ATP synthases^{4,5}. They use the energy released during ATP hydrolysis to pump protons across cellular membranes and are essential for acidification of intracellular organelles and for acid secretion^{1,3}. Accordingly, their function is important for a plethora of diverse cellular, physiological and pathological processes including membrane trafficking, signalling, kidney function and cancer metastasis³.

In neurons, arguably the most important role of the V-ATPase is energizing the loading of all neurotransmitters into synaptic vesicles (SVs)^{9–11}. In SVs, the V-ATPase hydrolyses ATP in the outward-facing soluble V₁ region and converts the released chemical energy into rotation of the transmembrane V₀ region that then translocates protons into the SV lumen through a coupling mechanism that is not well understood^{9,12} (Fig. 1a). The electrochemical proton gradient established by the V-ATPase subsequently energizes the secondary transport of all neurotransmitters into SVs^{9,11,13}.

Despite the absolutely essential role of V-ATPases in loading SVs with neurotransmitters, each SV contains only one or two copies of the

V-ATPase^{6,7}. Thus, any putative single-molecule-based stochasticity in the function of the V-ATPase may be expected to bear a disproportionately high impact on SV loading and neuronal communication. To shed more light on this bona fide single-molecule biological process, we monitored here, for the first time, to the best of our knowledge, electrogenic proton-pumping by the V-ATPase at the single-molecule level. Our measurements revealed three hitherto unknown ultralong-lived modes that underlie the function of V-ATPases: proton-pumping, inactive and proton-leaky. The regulation of V-ATPases by ATP and electrochemical gradients is based on switching between these modes, emphasizing their mechanistic importance in protein regulation.

Imaging of single brain SV_h

To preserve the proton-pumping activity of the mammalian-brain V-ATPase, which is not as stable as its bacterial homologues¹⁴, we avoided detergent solubilization protocols and instead isolated the endogenous V-ATPase in intact SVs purified from rat brain^{6,15} (Methods and Supplementary Fig. 1). Proton-pumping by the V-ATPase could

¹Center for Geometrically Engineered Cellular Membranes, Department of Chemistry, University of Copenhagen, Copenhagen, Denmark. ²Laboratory of Neurobiology, Max Planck Institute for Multidisciplinary Sciences, Göttingen, Germany. ³Institute for Auditory Neuroscience, University Medical Center, Göttingen, Germany. ⁴Multiscale Bioimaging Cluster of Excellence (MBExC), University of Göttingen, Göttingen, Germany. ⁵Department of Mathematical Sciences, University of Copenhagen, Copenhagen, Denmark. ⁶Cardiovascular Research Institute, Department of Pharmaceutical Chemistry, University of California San Francisco, San Francisco, CA, USA. ⁷Present address: Department of Mathematics, University of Manchester, Manchester, UK. ⁸Present address: Novozymes A/S, Kgs Lyngby, Denmark. ⁹These authors contributed equally: Christopher G. Shuttle, Julia Preobraschenski. [✉]e-mail: stamou@chem.ku.dk

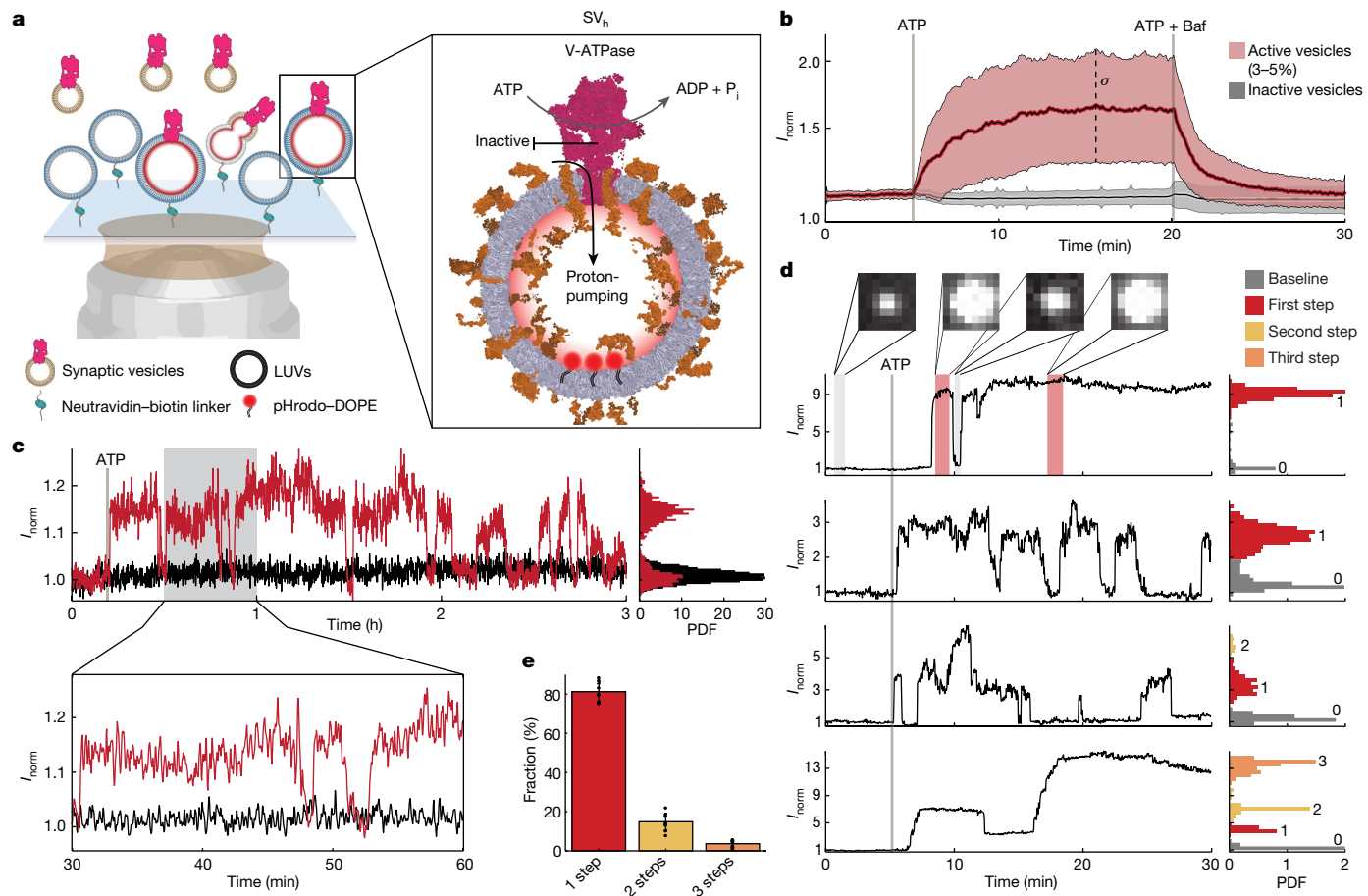


Fig. 1 | Ultralong measurements of proton-pumping into single SV_h reveal mode-switching of individual mammalian-brain V-ATPases. **a**, An illustration of the assay for single-transporter activity recordings. Proteoliposomes, carrying the pH-sensitive fluorophore pHrodo, syntaxin 1 and SNAP25, are immobilized on a glass slide. SVs containing mostly one copy of the V-ATPase are added in solution and fuse with the proteoliposomes, producing SV_h. On ATP hydrolysis, the V-ATPase pumps protons into the lumen of SV_h. **b**, Ensemble average of acidification kinetics from about 340 single SV_h (red) and about 10⁴ inactive vesicles (grey). The data are not corrected for photobleaching. Proton-pumping and vesicle acidification were initiated by addition of ATP and inhibited by 200 nM baflomycin. The solid lines are the mean; the shaded area corresponds to one standard deviation (s.d.). About 4% of vesicles showed ATP-dependent acidification. **c**, Left, an ultralong-term acidification trace of a representative

single SV_h revealing that the V-ATPase stochastically switches between long-lived proton-pumping and inactive modes (red trace). The black trace corresponds to a representative inactive vesicle. Right, histograms representing the corresponding distribution of intensities. PDF, probability density function.

d, The top two traces show SV_h with one acidification plateau corresponding to one active V-ATPase per SV_h. The bottom two traces are representative of SV_h with respectively two and three acidification plateaus, corresponding to two and three active V-ATPases. The kinetics have been processed by a Chung-Kennedy filter⁵⁴ for visual clarity, unless stated otherwise. **e**, Bar chart of the number of active V-ATPases per SV_h based on step-counting acidification plateaus; the average number is 1.2 ± 0.1 . The error bars correspond to one s.d. $n = 8$; hereafter, n is the number of independent experiments.

in principle be observed by measuring the luminal pH of SVs using genetically encoded pH sensors^{11,16}. However, the expression levels, quantum yield and photostability of these systems^{11,16} have historically been limiting the signal-to-noise ratio and duration of such recordings. Here, to observe the activity of the V-ATPase in single SVs for periods of up to 3 h, we incorporated 16–300 photostable synthetic pH indicators (DOPE–pHrodo) in the membrane of SVs, using a well-tested protocol of SNARE-mediated vesicle fusion¹⁷ (Methods, Supplementary Fig. 2 and Extended Data Figs. 1 and 2b).

As illustrated in Fig. 1a, we first tethered on a glass slide large unilamellar vesicles that contained DOPE–pHrodo and the SNARE acceptor complex, syntaxin 1 and SNAP25 (LUVs)¹⁸ (Methods). Subsequently, we injected SVs under conditions that we have previously demonstrated allow the fusion of predominantly one SV per LUV¹⁹ (Fig. 1a and Supplementary Figs. 1 and 3). The outcome was immobilized hybrid SVs (SV_h) containing DOPE–pHrodo and the entire SV proteome, including the endogenous V-ATPase (Fig. 1a). The mean membrane dilution during fusion was about 5.4-fold (Supplementary Fig. 2). As we and

others have shown, the low surface density allowed observation of single vesicles^{11,20} and the controlled tethering conditions preserved membrane permeability to ions^{20,21}, vesicle sphericity²² and the function of transmembrane proteins^{20,23,24}.

Proton-pumping by single V-ATPases

To activate the V-ATPase and initiate proton-pumping in the lumen of tethered SV_h, we added ATP. Three to five per cent of LUVs showed an ATP-specific decrease in luminal pH, suggesting that they had successfully fused with an SV (see ensemble-average trace (red) in Fig. 1b). The remaining majority (grey trace) did not respond to ATP addition. The pH plateau reached after about 15 min reflects a dynamic equilibrium between protons being actively pumped into the lumen and protons passively permeating through the membrane down the concentration gradient^{20,25}. Addition of the V-ATPase-specific inhibitor baflomycin (Fig. 1b; $t = 20$ min) blocked proton-pumping and collapsed completely and irreversibly the proton gradient in 100% of the acidified single SV_h.

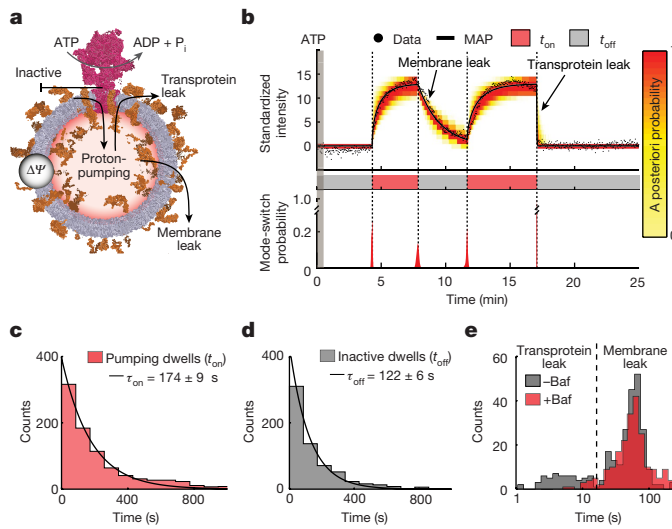


Fig. 2 | Dynamics of switching between the proton-pumping, inactive and proton-leaky modes. **a**, An illustration of different pathways for influx and efflux of protons in SV_h. Proton-pumping establishes a pH gradient and a membrane potential ($\Delta\Psi$). **b**, Analysis of stochastic fluctuations. Mode-switching events are detected on the intensity traces (black dots) using the a posteriori distributions (red histograms in bottom graph) and accepted when certainty is $>99\%$. Stochastic filtering techniques are then used on the segmented data to find the parameters with the highest likelihood given the exponential model (black line). The heat map represents the probability of where the signal is likely to be, given the observed data and the exponential model. The maximum a posteriori probability (MAP) of the signal is shown in black. **c,d**, Dwell time histograms for proton-pumping and inactive modes. Histograms were fitted with single exponentials. $n = 8$. **e**, Histogram of characteristic leakage lifetimes from the exponential fits shown in **b**. In the absence of bafilomycin, a fast and a slow component are observed with average leakage lifetimes of 6 s and 61 s. On addition of bafilomycin, the fast leakage pathway is blocked and can be thus attributed to the activated V-ATPase. $n = 15$.

In agreement with proteomic data⁶, this demonstrates that the V-ATPase is the only proton-pumping ATPase present in SVs and is solely responsible for the luminal acidification observed in our experiment.

We next tracked the ATP-specific acidification of SV_h at the single-particle level over periods of up to 3 h comprising about 10^5 proton turnovers⁸. Figure 1c and Extended Data Figures 1 and 2c show typical active single-SV_h traces in red and typical control single-SV_h traces in black. Strikingly, about 90% of active single SV_h exhibited reversible stochastic pauses in the acidification that remained hidden in the ensemble-average trace. In previous work with a P-type ATPase, we demonstrated that such pauses can be attributed directly to stochastic transitions of the transporter to long-lived inactive functional modes²⁰. To confirm that the acidification pauses we observe here are indeed due to switching-off of the V-ATPase and not due to stochastic switching-on of a large leakage current either from one of the other proteins present in the SV_h or from the membrane itself, we carried out the following control experiment. We imposed a pH gradient in the absence of ATP by exchanging the outside buffer and increasing the external pH by about 1 unit. This pH gradient resulted in an efflux of protons that we monitored in real time (Supplementary Fig. 4 and Supplementary Methods). Efflux kinetics followed a continuous monotonic decay in which no stochastic steps were observed. This finding confirms that when the V-ATPase is inactive there is no other proton-permeable pathway in the SV_h that can stochastically switch on or off. We considered the possibility that mode-switching is due to the reversible association of the V-ATPase with a hypothetical pumping-inhibitor, or a leakage activator; however, the systematic analysis of SV content^{6,7,26} does not suggest any plausible candidates, making this hypothesis unlikely. Thus, the

acidification pauses can be attributed to the V-ATPase reversibly switching between a long-lived proton-pumping mode and an inactive mode.

It is noteworthy that, as expected for a stochastic process, acidification is not synchronized between single SV_h (Extended Data Fig. 2). Thus, SV_h acidification comprises two distinct kinetic processes, intrinsic acidification (about 30 s) and mode-switching (about 1,000 s), that are typically convolved in ensemble-averaging experiments.

A ‘mode’ comprises a plethora of ‘conformations’ (for example, the continuous rotation taking place in the proton-pumping mode samples many discrete conformations^{2,27}) that can be sampled tens of thousands of times before reversibly switching to another mode. The structure(s) underlying the inactive mode we observed here are not known at present. It is thus unclear whether ATP hydrolysis continues while pumping is arrested^{12,28,29}. It is possible that they are early, reversible, steps in the conformational trajectory that ultimately leads to the complete dissociation of V₁ from V₀ (refs. 1,3). However, they are probably not related to the ADP-bound autoinhibited structures reported in the literature^{2,8,30} because mode-switching is not affected by ADP (Fig. 4e).

The ability to resolve stochastic mode-switching suggests the existence of a small number of single V-ATPase molecules per SV_h, in agreement with proteomic data⁶. As we have shown previously, the presence of more than one transporter per vesicle leads to multiple steps (or plateaus) in the acidification traces²⁰, similarly to having more than one ion channel in a membrane patch during a patch-clamp recording. Here we confirmed this also for the V-ATPase (Fig. 1d). Step analysis revealed that $81\% \pm 5\%$ of the active SV_h showed a single acidification plateau indicative of a single active V-ATPase, whereas $15\% \pm 5\%$ showed two plateaus, and $4\% \pm 2\%$ showed three or more plateaus (Fig. 1e). Apart from directly reporting the distribution of active V-ATPases per SV, our results also show that on average there are 1.2 ± 0.1 active V-ATPases per SV. This is in excellent agreement with the ensemble-average value of 1.4 measured by mass spectrometry⁶ and the average value of 1.27 ± 0.19 measured using fluorescent antibody labelling and single SV analysis⁷. These comparisons also suggest that about 85–95% of all V-ATPases are active. We restricted all subsequent analysis to SV_h containing a single active V-ATPase.

Active, inactive and proton-leaky modes

To quantify the dynamics of the transitions between modes, we developed a stochastic Bayesian event-detection model that allowed us to calculate maximum a posteriori probability estimates and distinguish with very high statistical certainty ($P > 0.99$) mode-switching events from background noise in the fluorescent signal (Fig. 2b, Supplementary Fig. 5 and Supplementary Discussion). Using the outputs of the stochastic model, we carried out a dwell time (t) analysis. Dwell time histograms were fitted well with single exponentials, suggesting that a single stochastic process underlies our observations and supporting the assertion that we observe the activity of single molecules (Fig. 2c,d). However, we cannot exclude the existence of other (faster or slower) modes outside the temporal resolution of our experiments. The characteristic dwell time of the pump (τ) in the proton-pumping mode was $\tau_{on} = 174 \text{ s} \pm 9 \text{ s}$ (Fig. 2c and Supplementary Fig. 6b, top row), and pumping was interrupted by intervals of inactivity, $\tau_{off} = 122 \text{ s} \pm 6 \text{ s}$ (Fig. 2d and Supplementary Fig. 6c, top row). As discussed in detail in Extended Data Fig. 5, about 30% of mode-switching events are faster than the time it takes for pH equilibration and thus do not plateau. Knowledge of the lifetimes allowed us to calculate the probability that the V-ATPase is in the proton-pumping mode, $P_{on} = 0.6 \pm 0.1$. The fact that the pump spends nearly half of the time switched off highlights the importance that modes outside the canonical pumping cycle bear for the function of V-ATPases. Ensemble-average experiments that assume the V-ATPase to pump continuously over time would underestimate pumping rates by about 170%.

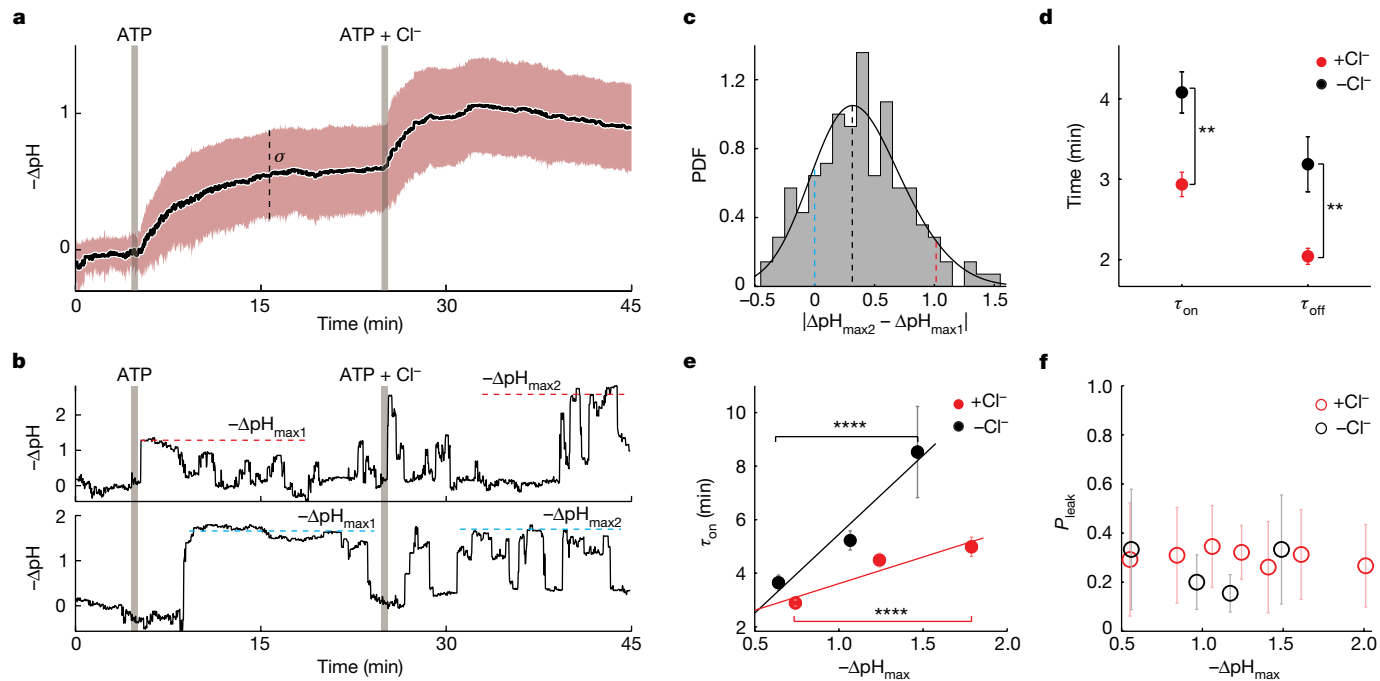


Fig. 3 | Mode-switching enables the regulation of the V-ATPase by electrochemical gradients. **a**, Ensemble average of acidification kinetics from about 220 single SV_h. The data are not corrected for photobleaching. Addition of choline chloride (+Cl⁻) collapsed the electrical component of the gradient ($\Delta\psi_{-Cl} > \Delta\psi_{+Cl}$). The black line is the mean; the red-shaded area corresponds to one s.d. $-\Delta pH$ is the difference between the initial and final pH. **b**, Representative examples of acidification kinetics of single SV_h. Maximal acidification ($-\Delta pH_{max}$) is defined as the average value of highest pH plateaus. **c**, Difference in $-\Delta pH_{max} \pm Cl^-$. The coloured dotted lines correspond to the traces in **b**, and the black line represents the mean. **d**, Characteristic dwell times for proton-pumping (τ_{on}) and inactive (τ_{off}) modes $\pm Cl^-$. The experiments used for dwell time determination were carried out independently (Supplementary Fig. 6). **P = 0.0012, two-sided Mann–Whitney U-test. The total number of active traces used is n = 117 ($-Cl^-$) and n = 467 ($+Cl^-$). The error bars correspond to the s.e. (95% confidence interval) of single exponential fits on the total population of dwell times. **e**, τ_{on} as a function of $-\Delta pH_{max} \pm Cl^-$. The data points and corresponding error bars have been produced by fitting single exponentials on equally sized subsets of the total population of dwell times. The total number of active traces used is n = 117 ($-Cl^-$) and n = 467 ($+Cl^-$). The error bars correspond to the s.e. (95% confidence interval) of the fits. ***P = 9 × 10⁻⁵ ($+Cl^-$, red) and ****P = 3 × 10⁻⁶ ($-Cl^-$, black), one-way ANOVA. **f**, Transproteins leak probability (P_{leak}) as a function of $-\Delta pH_{max}$. The data points correspond to the medians of equally sized subsets of the total dataset. The error bars correspond to one s.d. The total number of proton-leaky events used is n = 199 ($-Cl^-$) and n = 846 ($+Cl^-$). Pearson correlation coefficients showed no linear correlation ($\rho = -0.081$, P value = 0.25, $-Cl^-$; $\rho = 0.058$, P value = 0.09, $+Cl^-$).

active traces used is n = 117 ($-Cl^-$) and n = 467 ($+Cl^-$). The error bars correspond to the s.e. (95% confidence interval) of single exponential fits on the total population of dwell times. **e**, τ_{on} as a function of $-\Delta pH_{max} \pm Cl^-$. The data points and corresponding error bars have been produced by fitting single exponentials on equally sized subsets of the total population of dwell times. The total number of active traces used is n = 117 ($-Cl^-$) and n = 467 ($+Cl^-$). The error bars correspond to the s.e. (95% confidence interval) of the fits. ***P = 9 × 10⁻⁵ ($+Cl^-$, red) and ****P = 3 × 10⁻⁶ ($-Cl^-$, black), one-way ANOVA. **f**, Transproteins leak probability (P_{leak}) as a function of $-\Delta pH_{max}$. The data points correspond to the medians of equally sized subsets of the total dataset. The error bars correspond to one s.d. The total number of proton-leaky events used is n = 199 ($-Cl^-$) and n = 846 ($+Cl^-$). Pearson correlation coefficients showed no linear correlation ($\rho = -0.081$, P value = 0.25, $-Cl^-$; $\rho = 0.058$, P value = 0.09, $+Cl^-$).

To further investigate the mechanisms of proton efflux after the V-ATPase is switched off, we quantified the efflux kinetics by fitting them with a single exponential function. The histogram of characteristic efflux lifetimes in the presence of ATP revealed two separate peaks at 6 s \pm 0.5 s and 61 s \pm 0.5 s (Fig. 2e), demonstrating the existence of two distinct proton-leakage pathways in SV_h when the V-ATPase is active. We were able to attribute the larger lifetime (slow leakage) to passive leakage through the membrane because it coincided with the efflux lifetime in LUVs that did not contain any transporters. In agreement with this conclusion, SV_h leakage exhibited only passive leakage through the membrane when the V-ATPase was either inactive ($-ATP$) (Supplementary Fig. 4i,j) or specifically inhibited ($+bafilomycin$) (Fig. 2e). Thus, smaller leakage lifetimes (fast leakage) appear to be specific to active V-ATPases. We considered the possibility that leakage is due to reverse pumping occurring during ATP synthesis; however, the low concentration of adenosine diphosphate (ADP) in our samples owing to autohydrolysis of ATP (approximately nanomolar) makes this highly unlikely.

We thus conclude that the active V-ATPase can exit the cycle of conformational states involved in pumping and switch to modes that can be either inactive or proton-leaking (Fig. 2a). Furthermore, the transition from the inactive to the leaky mode seems to be forbidden because the leaky mode is not observed when the V-ATPase is inactive ($-ATP$ or $+bafilomycin$). Notably, the leakage mode is temporally distinct from the pumping mode. Thus, although the leakage mode reduces the ensemble-average (and time-average) pumping rates and the stoichiometry between ATP and net proton transport, it does not affect

the pumping rates or the stoichiometry of the pumping mode. The leakage mode is thus conceptually and mechanistically distinct from substrate slippage suggested to occur stochastically in the thermodynamic pumping cycles^{22,29}.

pH gradients regulate mode-switching

Although the biological purpose of the V-ATPase is to establish electrochemical proton gradients, little is known about gradient feedback on regulation of the pump^{1,3,13}. Single-molecule studies of detergent-reconstituted V-ATPase^{8,31} by definition cannot establish gradients, and ensemble-average measurements (for example, in fungal²⁹ or plant³² vacuole) cannot distinguish the individual contributions of pumping, inactive and leaky modes to regulation. Here we measured quantitatively the proton gradients of individual SV_h through an in situ single SV_h-based, pH calibration, and deconvolved these effects.

The pH calibration procedure is described in detail in Extended Data Fig. 3 and Supplementary Methods. In brief, to convert intensity to pH at the end of each experiment, we exchanged the bulk pH from 7.1 to 2.85 and added the protonophore CCCP to equilibrate the bulk and luminal pH. This gave us an accurate in situ measure of the maximal intensity response for each single SV_h, which we combined with ensemble-average measurements of the pK_a and the rate, to get a single SV_h-specific analytic function that we used to convert intensity to pH.

We first established a proton-mediated electrochemical membrane potential by adding only ATP, and subsequently we added chloride

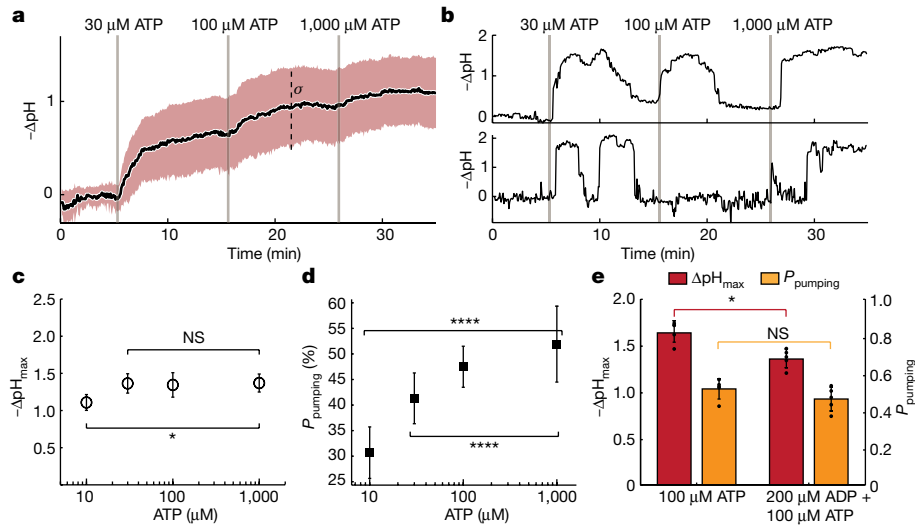


Fig. 4 | Regulation of functional modes by ATP and ADP. **a**, Ensemble average of acidification kinetics from 215 single SV_h at varying [ATP] in the presence of choline chloride. The black line corresponds to the mean; the red-shaded area corresponds to one s.d. **b**, Representative single-molecule traces. **c**, Mean maximal acidification ($-\Delta\text{pH}_{\text{max}}$) as a function of [ATP]. The error bars correspond to one s.d., $n=5, 4, 9$ and 9 for [ATP]=10, 30, 100 and 1,000 μM , respectively. NS, not significant ($P=0.94$); * $P=0.02$, one-way ANOVA. **d**, Probability that a molecule will be found in a pumping mode (P_{pumping}) as a function of [ATP]. The error bars correspond to one s.d., $n=7, 4, 4$ and 8 for [ATP]=10, 30, 100 and

1,000 μM , respectively. **** $P=1.1 \times 10^{-5}$ and **** $P=9 \times 10^{-14}$ for three and four ATP concentrations, respectively, one-way ANOVA. The pumping rates of the brain V-ATPase do not depend on ATP concentration. However, P_{pumping} is strongly regulated by substrate concentration. **e**, $-\Delta\text{pH}_{\text{max}}$ showed a slight decrease in the presence of 200 μM ADP at a 2:1 ratio of ADP/ATP. P_{pumping} is not affected by the presence of ADP in the system. The bars correspond to the mean and median for $-\Delta\text{pH}_{\text{max}}$ and P_{pumping} respectively, $n=5$. The error bars correspond to one s.d.* $P=0.016$ ($\Delta\text{pH}_{\text{max}}$); NS ($P=0.22$, P_{pumping}), two-sided Mann–Whitney U -test.

for charge compensation (Fig. 3a and Supplementary Fig. 7). Chloride counterions enter the vesicle lumen through chloride–proton antiport³³ and VGluT-mediated chloride influx^{18,34}, and negate positive charge buildup, thus releasing the electrical component of the gradient ($\Delta\Psi$) (that is, $\Delta\Psi_{-\text{Cl}} > \Delta\Psi_{+\text{Cl}} \approx 0$) (Supplementary Fig. 7a). Through a separate control experiment, we confirmed that chloride addition did not in itself introduce discernible acidification spikes (Supplementary Fig. 7b–d).

Ensemble-average measurements confirmed that the release of $\Delta\Psi$ regulates the V-ATPase and acidification on the average (Fig. 3a), in agreement with previous reports¹⁶. To deconvolve the pumping rates from the probability to be in the proton-pumping mode, we monitored acidification kinetics of single SV_h (Fig. 3b). This revealed, for the first time, to our knowledge, that releasing $\Delta\Psi$ indeed causes a bona fide increase in the (non-averaged) value of single SV_h maximal acidification ($\Delta\text{pH}_{\text{max}}$). The increase in maximal acidification ($|\Delta\text{pH}_{\text{max}2} - \Delta\text{pH}_{\text{max}1}|$) under the two conditions shows a broad distribution with a peak at about 0.3 pH units (Fig. 3c). We could thus verify that about 80% of the single molecules increased their pumping rates when $\Delta\Psi$ was released.

Notably, quantification of mode-switching dynamics also revealed potent regulation whereby the lifetimes of the proton-pumping mode (τ_{on}) and of the inactive periods (τ_{off}) were reduced respectively by 70% and 60% (Fig. 3d, Extended Data Fig. 4 and Supplementary Fig. 6b,c). Last, these measurements suggest that the steady-state value of $\Delta\text{pH}_{\text{max}} = 1$ that is quantified in ensemble-average measurements³⁵, such as in Fig. 3a, underestimates by about 180% the true maximal acidification values (Supplementary Fig. 7d) because it is weighted down by the periods of V-ATPase inactivity.

Next, we deconvolved the contribution of the electrical from the chemical part of the gradient to the regulation of τ_{on} . The τ_{on} value was positively correlated to increasing $\Delta\text{pH}_{\text{max}}$, indicating the existence of a positive feedback loop intrinsic to the V-ATPase, whereby increasing the proton gradient from 0.75 to 1.75 enhances τ_{on} by about 210% ($P < 0.0001$; Fig. 3e, red dots). The positive correlation of ΔpH and τ_{on} is not an artefact of slow buildup of chemical gradients, because the kinetics of pH buildup are nearly an order of magnitude faster than the durations of proton-pumping dwells (Extended Data Fig. 5). Increasing

$\Delta\Psi$ further reinforces the positive feedback, enhancing τ_{on} by about 280% ($P < 0.0001$; Fig. 3e, black dots). Thus, the pumping lifetime is positively correlated both to $\Delta\Psi$ and ΔpH . By contrast, the probability of the V-ATPase to switch to the proton-leaky mode was independent of ΔpH and $\Delta\Psi$ ($\rho = -0.081$ and $\rho = 0.058$; Fig. 3f). A proton-leaky mode has been directly observed before only for the eukaryotic H⁺-ATPase AHA2. However, in that case the probability to mode-switch was strongly regulated by proton gradients²⁰.

Knowledge of τ_{on} and τ_{off} allowed us to use transition state theory to calculate the activation barriers for transiting between the proton-pumping and the inactive modes in the presence or absence of chloride (Extended Data 6 and Supplementary Discussion). The two activation barriers are very large (about 86 kJ mol⁻¹), reflecting the stability of the conformations underlying the two long-lived modes that have dwell times of about 3 min (Fig. 3d). Chloride addition affects the forward and backward transitions nearly to the same extent; thus, the overall effect on the probability to mode-switch is negligible (Extended Data Fig. 6a). This suggests that regulation by electrochemical gradients manifests mainly by modulating the transition barrier but not the ground state of the two modes (Extended Data Fig. 6b). The regulation of the activation barrier is small (about 1 kJ mol⁻¹; Extended Data Fig. 6), revealing subtle structural rearrangements that however have a marked influence on the dwell time of the pumping mode (up to about 280%).

ATP regulates mode-switching

The availability of catalytic substrate (ATP) is of course essential for the proton-pumping activity of the V-ATPase. Early on, single-molecule rotation experiments directly observed how the rotation speed of the shaft (D subunit) was tuned by ATP concentration in a continuous Michaelis–Menten manner^{8,36}. However, these experiments did not measure proton-pumping and could thus not report how changes in the speed of ATP hydrolysis and rotation affect the proton current. Here, for the first time, to our knowledge, we tested at the single-molecule level the effect of ATP on proton-pumping.

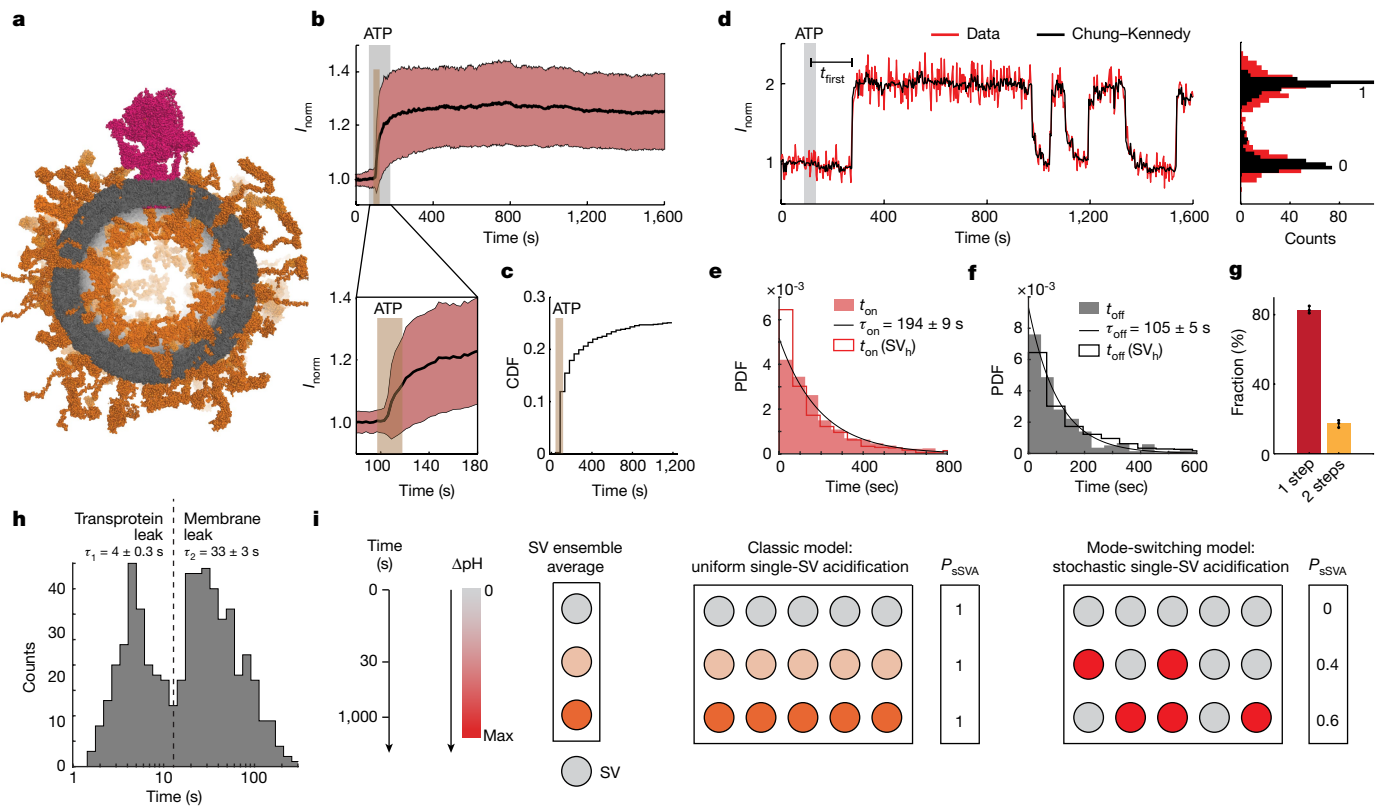


Fig. 5 | Mode-switching of the V-ATPase in intact SVs. **a**, A three-dimensional reconstruction of an intact SV. The V-ATPase is shown in magenta; all other SV proteins are shown in brown. **b**, Top: kinetics of ATP-dependent SV acidification, showing the ensemble average of about 950 single intact SVs (black line, mean value). The red-shaded area depicts one s.d. The data are corrected for photobleaching. Bottom: zoom-in to the first 80 s after ATP injection. $n = 3$. **c**, Cumulative histogram of the time elapsed until the stochastic occurrence of the first pumping event (t_{first}) after ATP injection. The stochastic activation of single V-ATPases (mode-switching kinetics) is convoluted in the ensemble-average acidification kinetics seen in **b**. CDF, cumulative distribution function. **d**, Left, representative single-SV acidification kinetics revealing mode-switching. Right, histogram of intensity revealing acidification plateaus

established by a single V-ATPase in an intact SV. **e,f**, Histograms of proton-pumping and resting dwell times (grey shade) were fitted with a single exponential (black line) to calculate the respective characteristic dwell times $\tau_{\text{on}} = 194 \pm 9$ s and $\tau_{\text{off}} = 105 \pm 5$ s (s.d. from the fit). Outlined histograms show the dwell time histograms of SV_h . **g**, Number of active V-ATPases in intact SVs as calculated by step analysis of acidification plateaus. The average SV contains about 1.20 ± 0.04 active V-ATPases. The error bars correspond to one s.d., $n = 3$. **h**, Proton-leakage lifetimes reveal a transprotein leak at 4 ± 0.3 s, as in SV_h . **i**, A schematic of the classical model of uniform single-SV acidification and the mode-switching model whereby single SVs acidify stochastically. At equilibrium, the probability that a random SV is acidified equals the probability that the V-ATPase is in the proton-pumping mode, $P_{\text{sSVA}} = P_{\text{pumping}} = 0.6$.

We explored a range of ATP concentrations from $10 \mu\text{M}$ to $1,000 \mu\text{M}$ because the Michaelis–Menten constant (K_m) of V-ATPases for ATP hydrolysis and rotation has been reported to be approximately $100 \mu\text{M}$ (ref. ³⁶). In agreement with previous reports, ensemble-average acidification kinetics showed an ATP-dependent increase in the ensemble-averaged proton-pumping and ΔpH (Fig. 4a and Supplementary Fig. 8a,b)¹⁶. To deconvolve the lifetime from the rate of the proton-pumping mode, we investigated acidification kinetics of single SV_h and followed mode-switching over time at different concentrations of ATP (Fig. 4b).

Paradoxically, the single-molecule experiments revealed that $\Delta\text{pH}_{\text{max}}$, and thus the single-molecule pumping rate, remain constant between $30 \mu\text{M}$ and 1mM ATP (Fig. 4c and Supplementary Fig. 8c–e). Crucially, the increase observed in ensemble-average proton-pumping experiments originates solely from an ATP-dependent regulation (up to 60%) of the probability (P_{pumping}) that the V-ATPase is in the proton-pumping mode (Fig. 4d and Extended Data Fig. 7). Thus, this broad range of physiologically relevant ATP concentrations regulated solely mode-switching.

The findings of these experiments suggest that coupling of shaft rotation to proton shuttling across the membrane becomes the dominant rate-limiting step in proton-pumping well below the K_m and that a further increase in the concentration of ATP results in futile cycles

of hydrolysis and rotation^{8,37}. The reduction of $\Delta\text{pH}_{\text{max}}$ at $10 \mu\text{M}$ ATP (Fig. 4c) suggests that hydrolysis becomes rate-limiting below $30 \mu\text{M}$ probably owing to diffusion-limited binding of ATP to the V-ATPase⁸.

To calculate the absolute maximal proton-pumping rate, we used a physical kinetic model that accounts for multiple parameters including passive and active ionic fluxes across the membrane, proton buffering in the lumen and buildup of membrane potential^{12,20,38}. The stochastic switching of the pump between pumping and inactive modes was extracted directly from the traces and used as time-dependent input to the model (Supplementary Discussion and Extended Data Fig. 8). We can thus estimate the maximal average pumping rate of the V-ATPase: $7 \pm 5 \text{ H}^+ \text{ s}^{-1}$.

The molecular mechanism underlying ATP-mediated regulation of P_{pumping} is not clear at present. We decided to test ADP–ATP competition because proton-pumping by V-ATPases was reduced by half in yeast vacuoles on addition of 5 mM ADP²⁹, and ADP has been reported to induce inhibitory rotation pauses to isolated subdomains of V-ATPases or F-type synthases^{30,31,39}. We initiated acidification of SV_h with $100 \mu\text{M}$ ATP, and after 20 min we added a twofold excess of ADP in the presence of 5 mM phosphate (Supplementary Fig. 9a,b). Our measurements revealed that competition by ADP caused a reduction (about 20%) of $\Delta\text{pH}_{\text{max}}$ and the pumping rates; however, it had no discernible influence on P_{pumping} (Fig. 4e and Supplementary Fig. 9c).

This suggests that although inhibition by ADP affects the proton-pumping mode, it is not responsible for mode-switching between pumping and inactive modes.

To summarize, in eukaryotes there are two closely related rotary mechanoenzymes whose function is tightly coupled to proton transport across membranes: the F-type synthases that harness the energy of proton gradients to synthesise ATP, and the V-type ATPases that hydrolyse ATP to pump protons and establish proton gradients. They have both been investigated by pioneering single-molecule experiments that directly observed rotation of the central rotor γ -subunit within the isolated F_1/V_1 domain and validated the mechanism of rotation^{8,40–42}; however, these experiments did not investigate proton transport. Two more recent articles investigated proton transport by single bacterial F_0F_1 -ATP synthases rotating backwards (that is, hydrolysing ATP)^{43,44}; however, the reported single-molecule pumping rates were averaged over periods of about 10 min, masking any putative stochasticity.

Here we present, for the first time, to our knowledge, rotary mechanoenzyme-mediated proton-pumping under electrogenic conditions that allowed direct observation of stochastic fluctuations in pumping rates. Our measurements revealed that the native mammalian-brain V-ATPase can exit the canonical proton-pumping mode and reversibly switch to physiologically relevant long-lived inactive and proton-leaky modes.

Mode-switching introduces marked all-or-none fluctuations in the electrochemical gradient of SV_h. However, further experiments motivated by anonymous reviewer comments revealed identical mode-switching phenotypes in intact SVs (Fig. 5). Figure 5i shows a schematic summarizing the features of the classical model of uniform single-SV acidification versus the mode-switching model. The classical paradigm assumes that the probability of single SV acidification is equal to one ($P_{\text{SSVA}} = 1$); that is, all individual SVs acidify simultaneously and continuously until they reach an equilibrium pH that is equal to the ensemble-average pH. By contrast, our measurements revealed that single SV acidification is stochastic and asynchronous, so that P_{SSVA} is time-dependent and ranges from 0 to 0.6; consequently, at any given moment at least 40% of SVs are not acidified.

Such all-or-none fluctuations in the electrochemical gradient of SVs would by definition regulate in a stochastic manner also proton-coupled secondary active neurotransmitter transporters and neurotransmitter loading to SVs¹¹, thus rationalizing the reports of heterogeneous neurotransmitter concentration in SVs⁴⁵. Notably, recent work demonstrated that most lysosomes in HeLa cells carry only one to four V-ATPases, suggesting that they may also be subject to stochastic fluctuations in acidification⁴⁶. In organelles comprising many transporters, mode-switching would not introduce as large fluctuations owing to ensemble averaging; it would however directly determine the mean value of the gradient.

More broadly, mode-switching, also referred to as long-lived disorder in reaction rates, seems to be a general property of enzymes; however, its biological role has been unclear^{47,48}. The observation that V-ATPase regulation by ATP and electrochemical gradients is based on mode-switching reveals a biological role of ultraslow mode-switching (disorder) in the regulation of protein function. Further elucidation of these phenomena will benefit greatly from direct, long-term, and where possible, simultaneous observation of conformational and functional dynamics, in conjunction with single-molecule-guided determination of cryo-electron microscopy structures^{20,24,49–53}.

Online content

Any methods, additional references, Nature Portfolio reporting summaries, source data, extended data, supplementary information, acknowledgements, peer review information; details of author contributions and competing interests; and statements of data and code availability are available at <https://doi.org/10.1038/s41586-022-05472-9>.

- Vasanthakumar, T. & Rubinstein, J. L. Structure and roles of V-type ATPases. *Trends Biochem. Sci.* **45**, 295–307 (2020).
- Ueno, H., Suzuki, K. & Murata, T. Structure and dynamics of rotary V1 motor. *Cell. Mol. Life Sci.* **75**, 1789–1802 (2018).
- Forgac, M. Vacuolar ATPases: rotary proton pumps in physiology and pathophysiology. *Nat. Rev. Mol. Cell Biol.* **8**, 917–929 (2007).
- Spikes, T. E., Montgomery, M. G. & Walker, J. E. Structure of the dimeric ATP synthase from bovine mitochondria. *Proc. Natl Acad. Sci. USA* **117**, 23519–23526 (2020).
- Okuno, D., Iino, R. & Noji, H. Rotation and structure of FoF1-ATP synthase. *J. Biochem.* **149**, 655–664 (2011).
- Takamori, S. et al. Molecular anatomy of a trafficking organelle. *Cell* **127**, 831–846 (2006).
- Mutch, S. A. et al. Protein quantification at the single vesicle level reveals that a subset of synaptic vesicle proteins are trafficked with high precision. *J. Neurosci.* **31**, 1461–1470 (2011).
- Furuike, S. et al. Resolving stepping rotation in *Thermus thermophilus* H⁺-ATPase/synthase with an essentially drag-free probe. *Nat. Commun.* **2**, 233 (2011).
- Abbas, Y. M., Wu, D., Bueler, S. A., Robinson, C. V. & Rubinstein, J. L. Structure of V-ATPase from the mammalian brain. *Science* **367**, 1240–1246 (2020).
- Rost, B. R. et al. Optogenetic acidification of synaptic vesicles and lysosomes. *Nat. Neurosci.* **18**, 1845–1852 (2015).
- Farsi, Z. et al. Single-vesicle imaging reveals different transport mechanisms between glutamatergic and GABAergic vesicles. *Science* **351**, 981–984 (2016).
- Grabe, M., Wang, H. & Oster, G. The Mechanochemistry of V-ATPase proton pumps. *Biophys. J.* **78**, 2798–2813 (2000).
- Gowrisankaran, S. & Milosevic, I. Regulation of synaptic vesicle acidification at the neuronal synapse. *IUBMB Life* **72**, 568–576 (2020).
- Dilworth, M. V., Findlay, H. E. & Booth, P. J. Detergent-free purification and reconstitution of functional human serotonin transporter (SERT) using disisobutylene maleic acid (DIBAM) copolymer. *Biochim. Biophys. Acta Biomembr.* **1863**, 183602 (2021).
- Ahmed, S., Holt, M., Riedel, D. & Jahn, R. Small-scale isolation of synaptic vesicles from mammalian brain. *Nat. Protoc.* **8**, 998–1009 (2013).
- Budzinski, K. L., Zeigler, M., Fujimoto, B. S., Bajjalieh, S. M. & Chiu, D. T. Measurements of the acidification kinetics of single Synaptophysin vesicles. *Biophys. J.* **101**, 1580–1589 (2011).
- Hernandez, J. M. et al. Membrane fusion intermediates via directional and full assembly of the SNARE complex. *Science* **336**, 1581–1584 (2012).
- Preobraschenski, J., Zander, J.-F., Suzuki, T., Ahnert-Hilger, G. & Jahn, R. Vesicular glutamate transporters use flexible anion and cation binding sites for efficient accumulation of neurotransmitter. *Neuron* **84**, 1287–1301 (2014).
- Castoroph, S. et al. Synaptic vesicles studied by dynamic light scattering. *Eur. Phys. J. E* **34**, 63 (2011).
- Vesaguri, S. et al. Direct observation of proton pumping by a eukaryotic P-type ATPase. *Science* **351**, 1469–1473 (2016).
- Stamou, D., Duschl, C., Delamarche, E. & Vogel, H. Self-assembled microarrays of attoliter molecular vessels. *Angew. Chem. Int. Ed.* **42**, 5580–5583 (2003).
- Bendix, P. M., Pedersen, M. S. & Stamou, D. Quantification of nano-scale intermembrane contact areas by using fluorescence resonance energy transfer. *Proc. Natl Acad. Sci. USA* **106**, 12341–12346 (2009).
- Mathiasen, S. et al. Nanoscale high-content analysis using compositional heterogeneities of single proteoliposomes. *Nat. Methods* **11**, 931–934 (2014).
- Fitzgerald, G. A. et al. Quantifying secondary transport at single-molecule resolution. *Nature* **575**, 528–534 (2019).
- Singh, A. et al. Protons in small spaces: discrete simulations of vesicle acidification. *PLoS Comput. Biol.* **15**, e1007539 (2019).
- Taofiqi, Z. et al. Hidden proteome of synaptic vesicles in the mammalian brain. *Proc. Natl Acad. Sci. USA* **117**, 33586–33596 (2020).
- Zhao, J., Benlekbir, S. & Rubinstein, J. L. Electron cryomicroscopy observation of rotational states in a eukaryotic V-ATPase. *Nature* **521**, 241–245 (2015).
- Drory, O. & Nelson, N. The emerging structure of vacuolar ATPases. *Physiology* **21**, 317–325 (2006).
- Kettner, C., Bertl, A., Obermeyer, G., Slayman, C. & Bihler, H. Electrophysiological analysis of the yeast V-type proton pump: variable coupling ratio and proton shunt. *Biophys. J.* **85**, 3730–3738 (2003).
- Kishikawa, J., Nakanishi, A., Furuike, S., Tamakoshi, M. & Yokoyama, K. Molecular basis of ADP inhibition of vacuolar (V)-type ATPase/synthase. *J. Biol. Chem.* **289**, 403–412 (2014).
- Uner, N. E. et al. Single-molecule analysis of inhibitory pausing states of V1-ATPase. *J. Biol. Chem.* **287**, 28327–28335 (2012).
- Davies, J. M., Hunt, I. & Sanders, D. Vacuolar H⁺-pumping ATPase variable transport coupling ratio controlled by pH. *Proc. Natl Acad. Sci. USA* **91**, 8547–8551 (1994).
- Accardi, A. Structure and gating of CLC channels and exchangers: structure and gating of CLC channels and exchangers. *J. Physiol.* **593**, 4129–4138 (2015).
- Schenck, S., Wojcik, S. M., Brose, N. & Takamori, S. A chloride conductance in VGLUT1 underlies maximal glutamate loading into synaptic vesicles. *Nat. Neurosci.* **12**, 156–162 (2009).
- Maycox, P. R., Deckwerth, T., Hell, J. W. & Jahn, R. Glutamate uptake by brain synaptic vesicles. Energy dependence of transport and functional reconstitution in proteoliposomes. *J. Biol. Chem.* **263**, 15423–15428 (1988).
- Minagawa, Y. et al. Basic properties of rotary dynamics of the molecular motor *Enterococcus hirae* V1-ATPase. *J. Biol. Chem.* **288**, 32700–32707 (2013).
- Imamura, H. et al. Evidence for rotation of V1-ATPase. *Proc. Natl Acad. Sci. USA* **100**, 2312–2315 (2003).
- Grabe, M. & Oster, G. Regulation of organelle acidity. *J. Gen. Physiol.* **117**, 329–344 (2001).
- Nakanishi, A., Kishikawa, J., Tamakoshi, M., Mitsuoka, K. & Yokoyama, K. Cryo EM structure of intact rotary H⁺-ATPase/synthase from *Thermus thermophilus*. *Nat. Commun.* **9**, 89 (2018).

Article

40. Yasuda, R., Noji, H., Yoshida, M., Kinosita, K. & Itoh, H. Resolution of distinct rotational substeps by submillisecond kinetic analysis of F₁-ATPase. *Nature* **410**, 898–904 (2001).
41. Noji, H., Yoshida, M. & Kinosita, K. Direct observation of the rotation of F₁-ATPase. *Nature* **386**, 299–302 (1997).
42. Adachi, K. et al. Coupling of rotation and catalysis in F1-ATPase revealed by single-molecule imaging and manipulation. *Cell* **130**, 309–321 (2007).
43. Watanabe, R. et al. Arrayed lipid bilayer chambers allow single-molecule analysis of membrane transporter activity. *Nat. Commun.* **5**, 4519 (2014).
44. Soga, N. et al. Monodisperse liposomes with femtoliter volume enable quantitative digital bioassays of membrane transporters and cell-free gene expression. *ACS Nano* **14**, 11700–11711 (2020).
45. Phan, N. T. N., Li, X. & Ewing, A. G. Measuring synaptic vesicles using cellular electrochemistry and nanoscale molecular imaging. *Nat. Rev. Chem.* **1**, 0048 (2017).
46. Maxson, M. E. et al. Detection and quantification of the vacuolar H⁺ATPase using the *Legionella* effector protein SidK. *J. Cell Biol.* **221**, e202107174 (2022).
47. Lu, H. P., Xun, L. & Xie, X. S. Single-molecule enzymatic dynamics. *Science* **282**, 1877–1882 (1998).
48. Ciftci, D. et al. Single-molecule transport kinetics of a glutamate transporter homolog shows static disorder. *Sci. Adv.* **6**, eaaz1949 (2020).
49. Akyuz, N., Altman, R. B., Blanchard, S. C. & Boudker, O. Transport dynamics in a glutamate transporter homologue. *Nature* **502**, 114–118 (2013).
50. Erkens, G. B., Hänel, I., Goudsmit, J. M. H., Slotboom, D. J. & van Oijen, A. M. Unsynchro nised subunit motion in single trimeric sodium-coupled aspartate transporters. *Nature* **502**, 119–123 (2013).
51. Akyuz, N. et al. Transport domain unlocking sets the uptake rate of an aspartate transporter. *Nature* **518**, 68–73 (2015).
52. Dyla, M. et al. Dynamics of P-type ATPase transport revealed by single-molecule FRET. *Nature* **551**, 346–351 (2017).
53. Rundlet, E. J. et al. Structural basis of early translocation events on the ribosome. *Nature* **595**, 741–745 (2021).
54. Chung, S. H. & Kennedy, R. A. Forward-backward non-linear filtering technique for extracting small biological signals from noise. *J. Neurosci. Methods* **40**, 71–86 (1991).

Publisher's note Springer Nature remains neutral with regard to jurisdictional claims in published maps and institutional affiliations.

Springer Nature or its licensor (e.g. a society or other partner) holds exclusive rights to this article under a publishing agreement with the author(s) or other rightsholder(s); author self-archiving of the accepted manuscript version of this article is solely governed by the terms of such publishing agreement and applicable law.

© The Author(s), under exclusive licence to Springer Nature Limited 2022

Methods

Chemicals

Phospholipids and cholesterol were purchased from Avanti Polar Lipids. Chemicals for buffers, detergents and other reagents were purchased from Sigma-Aldrich, unless stated otherwise.

The lipid-conjugated pH sensor PE-pHrodo

The lipid-conjugated pH sensor PE-pHrodo was synthesized by linking DOPE to the pHrodo red ester reagent (Invitrogen). Synthesis, purification and characterization of its properties as a function of pH are previously described⁵⁵.

Protein expression and purification

The stabilized syntaxin–SNAP25 acceptor complex (ΔN complex) constructs consist of the pETDuet-1 vector carrying syntaxin 1A (183–288) and the carboxy-terminal fragment of synaptobrevin 2 (49–96) and the pET28a vector carrying His₆-tagged SNAP25A (refs. ^{56,57}) and originate from *Rattus norvegicus*. The components of the ΔN complex, syntaxin 1A (183–288), synaptobrevin 2 (49–96) and SNAP25A were coexpressed in *Escherichia coli* BL21(DE3) and purified as previously described^{56,57}. In brief, the cells were lysed, and the complex was extracted using 10% Na cholate (w/v) in 4 M urea, 500 mM NaCl, 20 mM HEPES, pH 7.4 and 8 mM imidazole. The non-dissolved particles were separated by centrifugation, and the cleared lysate was subjected to Ni²⁺-NTA affinity purification. Finally, the complex was further purified by anion-exchange chromatography in the presence of 2% CHAPS using the ÄKTA system (GE Healthcare), flash frozen and stored at –80 °C until use.

Proteoliposome preparation and characterization

Proteoliposomes were prepared by mixing the detergent-solubilized ΔN complex together with lipids and subsequently removing the detergent by dialysis^{58,59}. In detail, the synthetic lipid mix consisting of 1,2-dioleoyl-sn-glycero-3-phosphocholine (DOPC), 1,2-dioleoyl-sn-glycero-3-phospho-L-serine (DOPS; both Avanti Polar Lipids), cholesterol (from sheep wool, Avanti Polar Lipids), 1,2-dioleoyl-sn-glycero-3-phosphoethanolamine-N-(cap biotinyl) (18:1 Biotinyl Cap PE, Avanti Polar Lipids) and DOPE-pHrodo (see above) at a molar ratio of DOPC/DOPS/cholesterol/(18:1 Biotinyl Cap PE)/DOPE-pHrodo 64.4:10:25:0.5:0.1 was formed by evaporating the organic solvent from the lipids and dissolving the dried film in 300 mM glycine, 2 mM MOPS-Tris, pH 7.3, 2 mM MgSO₄, 5% n-octyl- β -D-glucopyranosid to a concentration of 10 mg ml^{−1} lipids. The protein/lipid ratio (mol/mol) was adjusted to 1:600, amounting to approximately 130 complexes per liposome that, as earlier controls have shown⁶⁰, are preferentially oriented towards the outside of the liposome. The final lipid concentration was adjusted to 4 mM. After mixing, the respective solutions were dialysed in Slide-A-Lyzer dialysis cassettes (2 kDa MWCO, Thermo Scientific) overnight at 4 °C in 300 mM glycine, 2 mM MOPS-Tris, pH 7.3 and 2 mM MgSO₄. The dialysis buffer was also supplemented with 2 g BioBeads (BioRad) per litre of buffer to adsorb detergent monomers. After dialysis, liposomes were aliquoted, flash frozen and stored at –80 °C until use. Before use, proteoliposomes were subjected to sequential extrusion through 800-nm- and 200-nm-size nucleopore polycarbonate membranes mounted on a mini extruder (Avanti Polar Lipids).

SV_h from rat brain

SV_hs were isolated from rat brain according to previous publications^{6,61,62}. In brief, an SV-enriched fraction, LP2, was prepared by differential centrifugation and subjected to continuous sucrose density gradient centrifugation. The part between 0.04 and 0.4 M sucrose (coloured) was collected and additionally separated by chromatography on controlled-pore glass beads. After the size-exclusion

chromatography, the SVs were pelleted by ultracentrifugation, resuspended in 320 mM sucrose and 5 mM HEPES, pH 7.4, flash frozen and stored at –80 °C until use. For more details, see Supplementary Fig. 1a. The protein concentration range varied from 1.5 mg ml^{−1} to 2.5 mg ml^{−1}.

The purified SV fraction contains a mixture of all SVs present in the cerebral cortex. Recently, the distribution of all known vesicular neurotransmitter transporters has been quantified in this preparation⁶³. Accordingly, close to 80% of SVs are glutamatergic and 15% are GABA-ergic, confirming the findings of an earlier study⁶⁴. Vesicles containing other transporters (for dopamine, acetylcholine and so on) contribute only a few per cent, with the exception of the Zn²⁺ transporter ZnT3, which colocalizes with about a third of the glutamatergic vesicles⁶³.

Adult Wistar rats were purchased from Charles River Laboratories, or Janvier, and were kept until 5 to 6 weeks of age at a 12/12-h light/dark cycle with food and water ad libitum. A certificate of approval for using animals was issued by the Landkreis Göttingen Office of Veterinary Affairs and Consumer Protection.

Ensemble-average ATPase assay

The activity of each preparation of SVs and pHrodo-labelled proteoliposomes was assessed by generating hybrid SVs as previously described^{18,65} and measuring chloride-dependent acidification of the hybrid SVs in a bulk assay using pHrodo as a pH-sensitive probe. In brief, 60 μ l pHrodo-labelled + ΔN liposomes were preincubated with 10 μ l of SVs ($c = 2$ mg ml^{−1}) for 45 min at room temperature. Subsequently, the acidification of the pHrodo-labelled hybrid SVs was monitored by measuring changes in fluorescence at 590 nm (slits: 3 nm for excitation at 560 nm and 5 nm for emission at 590 nm) in a fluorimeter (Fluoromax-2, Horiba) at 37 °C. Typically, 930 μ l buffer (300 mM glycine, 30 mM choline chloride, 2 mM MOPS-Tris, pH 7.3, 2 mM MgSO₄) was mixed in a cuvette with 70 μ l SV_h. The acidification reaction was started by adding 2 mM MgATP and stopped by adding 20 mM (NH₄)₂SO₄. Representative traces are shown in Supplementary Fig. 3.

Surface preparation and immobilization of + ΔN proteoliposomes

Surfaces were prepared according to previously published protocols^{20,23}. In brief, glass slides of thickness 0.17 ± 0.01 mm were passed through sequential sonication cycles with 2% (v/v) Helmanex III, MilliQ and subsequently rinsed with 99% (v/v) ethanol and 99% (v/v) methanol. Then, the slides were dried under nitrogen flow and plasma-etched for 3 min to remove impurities. The glass slide was attached to Ibidi sticky slides VI 0.4. The surface was functionalized by first incubating a mixture of 100:1 PLL-g-PEG and PLL-g-PEG-biotin at 1 mg ml^{−1} (SuSoS) for 30 min and then washed away with a 15 mM HEPES buffer. A 0.1 mg ml^{−1} concentration of Neutravidin in 15 mM HEPES buffer was then incubated for 10 min and flushed out using the activity buffer (300 mM glycine, 2 mM MOPS, 2 mM MgSO₄, pH 7.1 at 23 °C; the pH was adjusted with Tris). Once the flow chamber had equilibrated with the activity buffer, we exchanged the buffer with the proteoliposome solution (proteoliposomes in activity buffer) and incubated until reaching a density of approximately 1,000 immobilized liposomes in a 81.92 μ m × 81.92 μ m field of view. Subsequently, non-immobilized vesicles were flushed away.

SV_h formation

Purified SVs were thawed, diluted (1:100) and incubated in the activity buffer for 5–10 min. After LUVs + ΔN (hereafter referred to as LUVs) were immobilized on the functionalized glass surface and spatially separated, SVs were injected into the flow chamber containing the LUVs allowing for the fusion reaction to commence. Typically, incubation of SVs in the flow chamber lasted approximately 45 min. SV_h were prepared using the aforementioned method in all experiments apart from the

Article

ones shown in Figs. 1c and 2e, in which the fusion reaction was carried out in solution, in Eppendorf tubes, by mixing the populations of SVs and LUVs and allowing for 45-min incubation. Then, SV_h were directly immobilized onto the glass surface.

Lipid incorporation into intact SVs

To image the acidification kinetics of single intact SVs, we established a protocol to incorporate lipid molecules into the native membranes of SVs. First, we dissolved 10 µl pHrodo-DOPE (1 mg ml⁻¹) and 5 µl DSPE-PEG(2000)-biotin (10 mg ml⁻¹) in 85 µl of chloroform. Then, we formed a lipid film by evaporation of chloroform under nitrogen flow. The lipid film was then placed under vacuum for at least 30 min to remove traces of solvent. Subsequently, the lipid film was rehydrated in 20 µl of SVs diluted in 80 µl of activity buffer and mixed initially with repeated pipetting. Once the lipid film was dissolved, we shook the sample for 30 min at 600 rpm and 37 °C. Finally, we spun down non-hydrated debris at 13,000 r.p.m. for 1 min and removed SVs without disturbing the pellet. The sample was then distributed into 10-µl aliquots and freeze-thawed before use. To image SVs, we immobilized them on a functionalized glass using the same protocols as for SV_h imaging. Once immobilized, the activity of the V-ATPase was triggered on addition of ATP. Single-molecule proton-pumping data are shown in Fig. 5.

Image acquisition

All fluorescence microscopy was performed on a commercial Olympus total internal reflection fluorescence microscope (Olympus Europa). We used the EMCCD camera iXon 897 (Andor Technology). Excitation of fluorophores was achieved using an Olympus Cell solid-state laser emitting at 532 nm. The microscope was equipped with an Olympus total internal reflection fluorescence UApoN ×100, 1.49 NA, oil immersion objective. The microscope was able to maintain focus for extended periods of time using the continuous function of the Zero Drift Correction module built into the microscope. A 532/10 excitation bandpass filter was used for fluorophore excitation. An emission filter with a bandpass 582.5/75 and a beamsplitter bandpass 585/75 were used to block fluorophore excitation. Image acquisition software linked to the microscope and used throughout this article was for the most part Olympus xcellence rt (version 2.0) and to a lesser extent Olympus cellSens (version 3.2).

Replicates of measurements for each condition were taken on the same sample measured repeatedly throughout the present manuscript.

Reporting summary

Further information on research design is available in the Nature Portfolio Reporting Summary linked to this article.

Data availability

The data that support the findings of this study are available from the corresponding author upon request. Source data are provided with this paper.

Code availability

Source code and a demo for the Bayesian filtering algorithm that was used for the detection of events can be found at https://github.com/pete906/Bayesian_Filtering_Proton_Pump.git. Support on the use of the algorithm can be provided by the corresponding author upon reasonable request.

55. Kemmer, G. C. et al. Lipid-conjugated fluorescent pH sensors for monitoring pH changes in reconstituted membrane systems. *Analyst* **140**, 6313–6320 (2015).
56. Pobatti, A. V. N- to C-terminal SNARE complex assembly promotes rapid membrane fusion. *Science* **313**, 673–676 (2006).
57. Stein, A., Radhakrishnan, A., Riedel, D., Fasshauer, D. & Jahn, R. Synaptotagmin activates membrane fusion through a Ca²⁺-dependent *trans* interaction with phospholipids. *Nat. Struct. Mol. Biol.* **14**, 904–911 (2007).
58. Rigaud, J.-L., Lévy, D. & Düzunges, N. (ed.) in *Methods in Enzymology* Vol. 372, 65–86 (Elsevier, 2003).
59. Rigaud, J.-L., Pitard, B. & Levy, D. Reconstitution of membrane proteins into liposomes: application to energy-transducing membrane proteins. *Biochim. Biophys. Acta Bioenerg.* **1231**, 223–246 (1995).
60. van den Bogaart, G. et al. One SNARE complex is sufficient for membrane fusion. *Nat. Struct. Mol. Biol.* **17**, 358–364 (2010).
61. Huttner, W. B., Schiebler, W., Greengard, P. & De Camilli, P. Synapsin I (protein I), a nerve terminal-specific phosphoprotein. III. Its association with synaptic vesicles studied in a highly purified synaptic vesicle preparation. *J. Cell Biol.* **96**, 1374–1388 (1983).
62. Nagy, A., Baker, R. R., Morris, S. J. & Whittaker, V. P. The preparation and characterization of synaptic vesicles of high purity. *Brain Res.* **109**, 285–309 (1976).
63. Upmanyu, N. et al. Colocalization of different neurotransmitter transporters on synaptic vesicles is sparse except for VGLUT1 and ZnT3. *Neuron* **110**, 1483–1497 (2022).
64. Takamori, S., Riedel, D. & Jahn, R. Immunoisolation of GABA-specific synaptic vesicles defines a functionally distinct subset of synaptic vesicles. *J. Neurosci.* **20**, 4904–4911 (2000).
65. Preobraschenski, J. et al. Dual and direction-selective mechanisms of phosphate transport by the vesicular glutamate transporter. *Cell Rep.* **23**, 535–545 (2018).

Acknowledgements We thank S.C. Blanchard for conversations, H. Grubmüller, C. Kutzner and P.E. Gourdon for providing and helping with visualizations of the SV. This work was supported by the Novo Nordisk Foundation (grant NNF17OC0028176), the Villum Foundation (grants 17617 and 17646) and the Lundbeck Foundation (grant R249-2017-1406 to E.K. and R250-2017-1175 to S.V.), and a grant from the European Research Council to R.J. (SVNeuroTrans). M. Grabe and F.M. were supported by NIH R01-AG057342. J.P. was financially supported by the Deutsche Forschungsgemeinschaft (German Research Foundation) under Germany's Excellence Strategy EXC 2067/1-390729940.

Author contributions D.S. conceived the strategy and was responsible for project management and supervision. E.K., J.P. and D.S. designed research with initial help from S.V. E.K. developed the single-molecule assay and collected and analysed all data. C.G.S. was the principal software developer. J.P. prepared all biochemical samples, with help from M. Ganzella, under the supervision of R.J. P.J.J and J.L.P. developed the stochastic event-detection model and estimations. J.H. collected the data for Fig. 5h. M.P.M. established the pH calibration. M. Grabe and F.M. developed the non-equilibrium physical model. O.M. simulated the spatial distribution of vesicles. D.S. and E.K. wrote the main text. E.K. prepared all figures and Supplementary Information. All authors discussed the results and commented on the manuscript.

Competing interests The authors declare no competing interests.

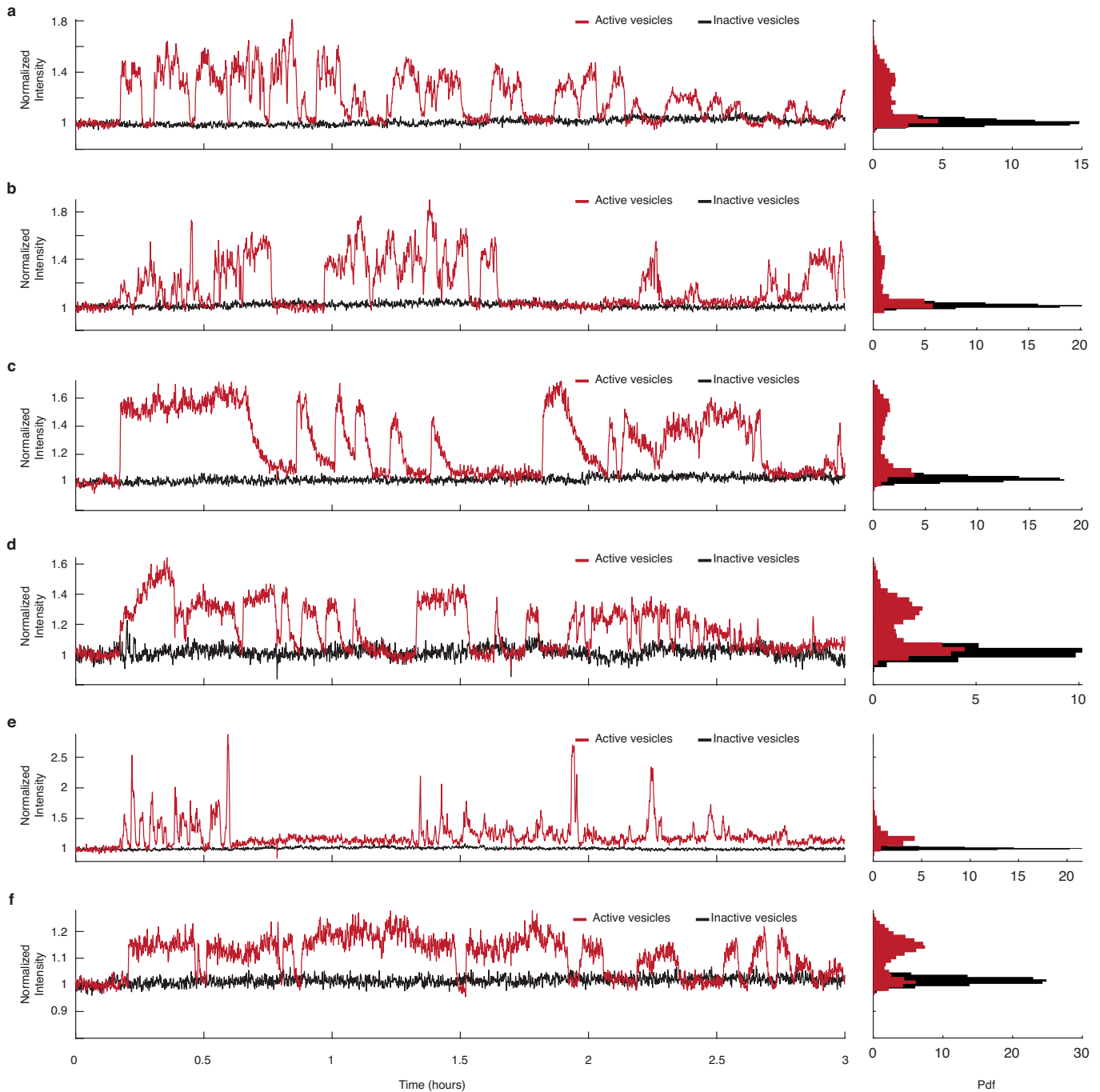
Additional information

Supplementary information The online version contains supplementary material available at <https://doi.org/10.1038/s41586-022-05472-9>.

Correspondence and requests for materials should be addressed to Dimitrios Stamou.

Peer review information *Nature* thanks Ken Yokoyama and the other, anonymous, reviewer(s) for their contribution to the peer review of this work. Peer reviewer reports are available.

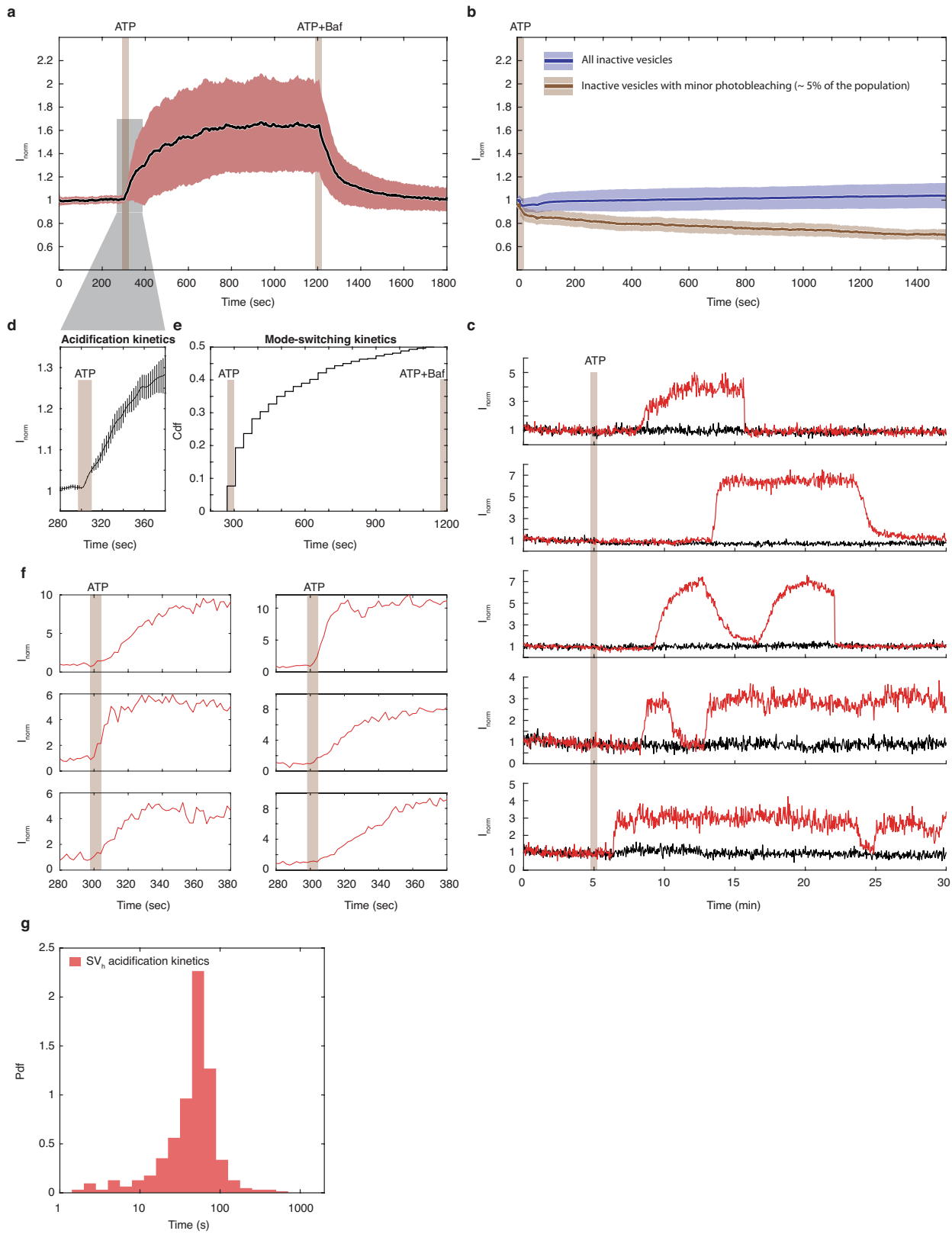
Reprints and permissions information is available at <http://www.nature.com/reprints>.



Extended Data Fig. 1 | Ultralong-term activity recordings of the V-ATPase in single SV_h. Activity recordings that spanned the duration of three hours revealed mode-switching of single V-ATPases. Each liposome can contain up to hundreds of fluorophores and the system has been optimized for minimal photon budget usage, therefore minimizing photobleaching. **a–f,** Left panels: Representative single molecule acidification kinetics displaying long-lived proton pumping and inactive modes. Activity was initiated upon addition of ATP.

Red traces correspond to active vesicles that have been normalized to the baseline. Black traces correspond to inactive vesicles. The data has not been corrected for photobleaching. A mild linear filter has been used in the visualization of these traces. Right panels: Histograms of acidification plateaus. Red histograms correspond to active vesicles while black histograms correspond to inactive vesicles.

Article

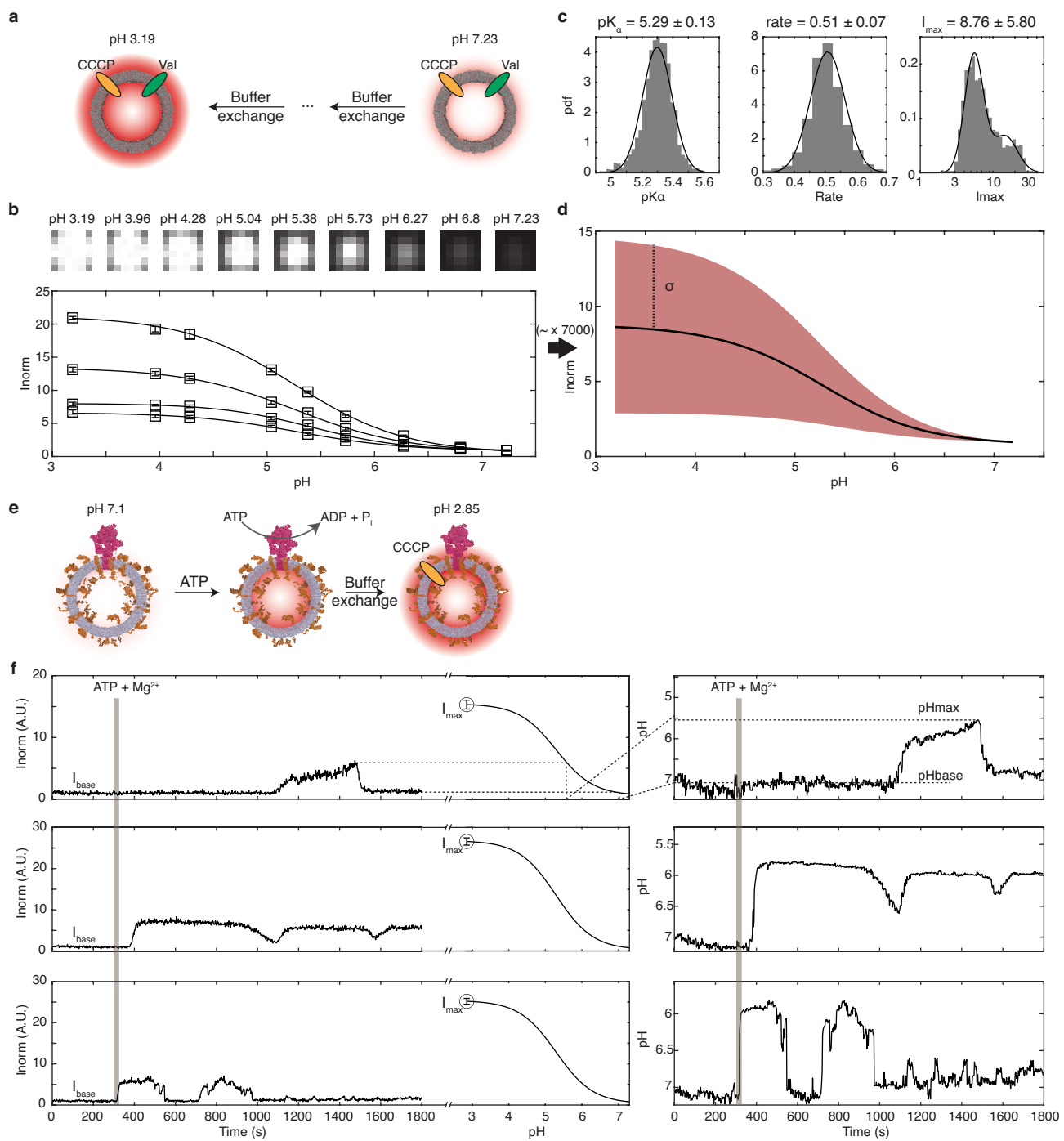


Extended Data Fig. 2 | See next page for caption.

Extended Data Fig. 2 | Single-vesicle acidification kinetics are fast (~ 30 s), the slow apparent ensemble average acidification kinetics are governed by slow mode-switching (~ 1000 s). Under our imaging conditions we never observe single-molecule photo-blinking or photo-bleaching. **a**, Ensemble average acidification kinetics of single SV_h. Solid black line corresponds to the mean acidification. Red shaded area corresponds to one s.d. of all single vesicle traces. Note: this figure is also shown in Fig. 1b. **b**, Solid lines correspond to the mean while shaded areas correspond to one s.d. The majority of inactive single vesicle traces (~ 95% of the population) showed photostability with no indication of photobleaching or self-quenching. ~ 5% of the vesicles showed signs of minor photobleaching on the order of 30% after 25 min of recording. We never observed an increase in fluorescent intensity while imaging which would be indicative of self-quenching. **c**, Collections of active and inactive

vesicles. Inactive vesicles retained stable baseline signals throughout the course of experiments. No photoblinking was observed for the totality of inactive vesicles **d**. Ensemble average acidification kinetics immediately after ATP injection. Black line corresponds to the mean, $n = 4$. Error bars correspond to one s.d., $n = 4$. Acidification until the dynamic equilibrium of pumping and leakage is reached takes place in the order of tens of seconds, consistent with previous ensemble measurements of acidification. **e**, Cumulative histogram of the time elapsed until the onset of the first proton-pumping event. Mode-switching dynamics are slow (~ 1000 seconds) and are responsible for the slow kinetics seen in the ensemble average traces in **a**. **f**, Zoom in regions of representative single-vesicle traces showcase that acidification occurs in the order of tens of seconds. **g**, Histogram of single-vesicle acidification kinetics shows that most vesicles acidify in 10-100 s.

Article



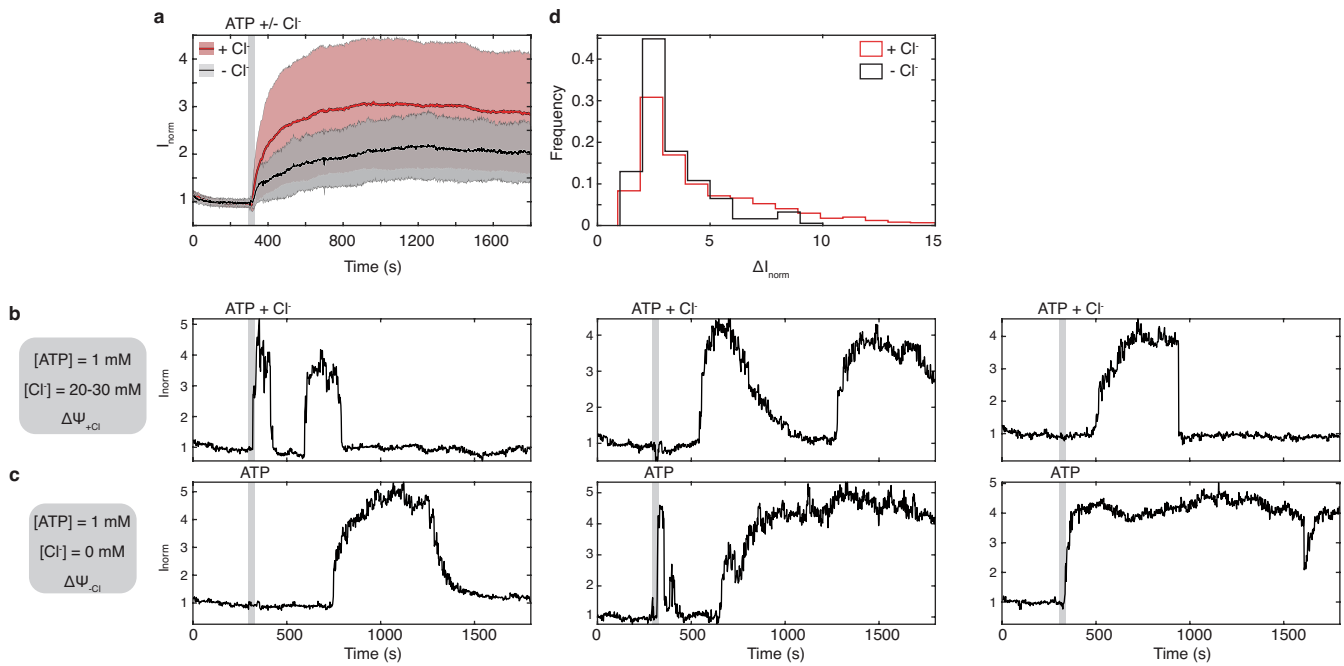
Extended Data Fig. 3 | See next page for caption.

Extended Data Fig. 3 | pH calibration methodology for single molecule activity data.

a, Schematic illustration of *pH* calibration experiments. LUVs are incubated in a K-gluconate-MOPS buffer at *pH* 7.23 in the presence of valinomycin and CCCP to equilibrate chemical gradients. Subsequent injection of the same buffer (including valinomycin and CCCP) at decreasing *pH* concentrations leads to equilibrated acidification of both the lumen and the extraluminal space around the vesicles. The *pH* changes are reported as an increase in fluorescence. **b**, Representative examples of single vesicle calibration data. Data has been normalized to the activity baseline value (see supplementary text). Each vesicle reports a change in fluorescence as a function of *pH* which is then fitted with a sigmoidal function. Values correspond to the mean fluorescence for a stack of 20 images. Error bars represent one s.d. of fluorescence intensity for a stack of 20 images. **c**, Distributions of the sigmoidal fit parameters. The dissociation constant and growth rate of the vesicles show a normally distributed population with very narrow standard deviations. The fluorescence, I_{max} , at saturating *pH*, however showed a larger spread. Thus, the dissociation constant and the

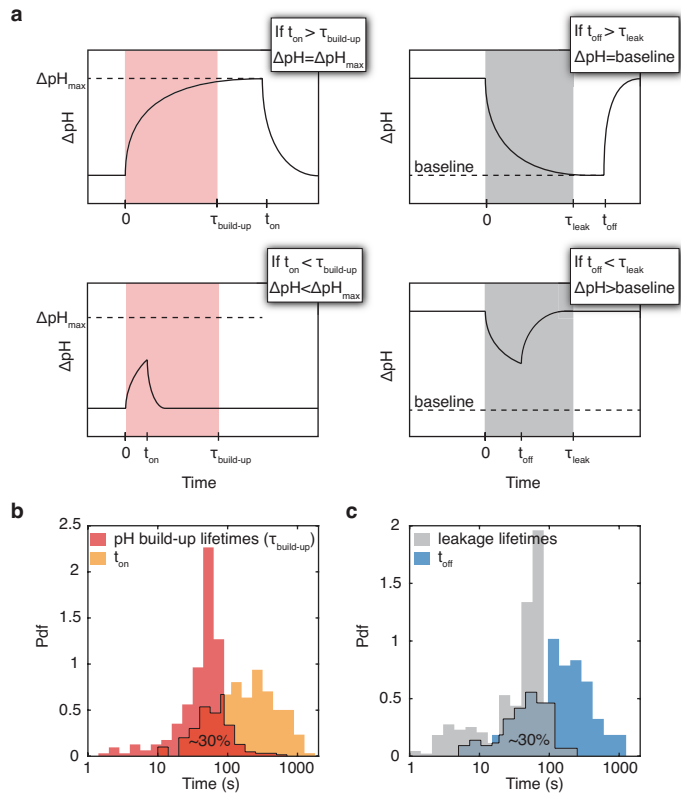
growth rate are globally determined from these experiments while the I_{max} saturation value is locally determined for SV_h post activity. **d**, Ensemble average of sigmoidal fits for the entire population of vesicles. Black line corresponds to the mean while red-shaded area corresponds to one s.d. of the population. **e**, Illustration of the typical process during activity measurements. After recording a baseline, ATP is injected into the system and V-ATPase activity is triggered. After the end of the activity recording, the SV_h are treated with activity buffer at signal saturating *pH* 2.85 including CCCP and chloride to allow for influx of protons and chloride counterions to determine I_{max} locally for each vesicle. **f**, Example activity traces and their corresponding calibration curve determined by the global dissociation constant, the global growth rate (determined in panel (c)), the local baseline and saturation values, I_{base} and I_{max} , respectively. Henceforth, normalized intensities of activity measurements can be mapped onto corresponding *pH* values, as shown in the right-hand side traces. At saturation the data points correspond to the mean fluorescence for a stack of 20 images. Error bars represent one s.d. of fluorescence intensity for a stack of 20 images.

Article



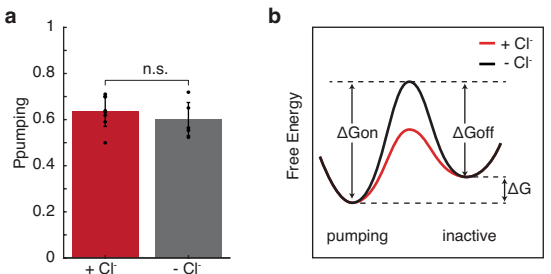
Extended Data Fig. 4 | Single vesicle acidification kinetics in the presence and absence of chloride. Data analysed in these experiments was used to determine dwell times for both proton-pumping and inactive modes and their relation to electrochemical gradients (Fig. 2c,d, Fig. 3d–f). a, Ensemble average acidification kinetics of SV_h. In the absence of chloride, a membrane potential clamps the activity of the V-ATPase (black line). When 30 mM choline chloride is introduced, the potential is released and the V-ATPase can establish larger

gradients (red line) (also see Fig. 3a, b). Shaded areas correspond to one s.d. b,c, Typical single molecule traces for the different conditions investigated in these experiments. d, Histograms of maximum intensities of single molecule data. Data shows different distribution of signals. The number of independent experiments were $n = 8$ for data in the presence of chloride (Panel (a), (d); Red data and Panel (b)) and $n = 5$ for data in the absence of chloride (Panel (a), (d); Black data and Panel (b)).



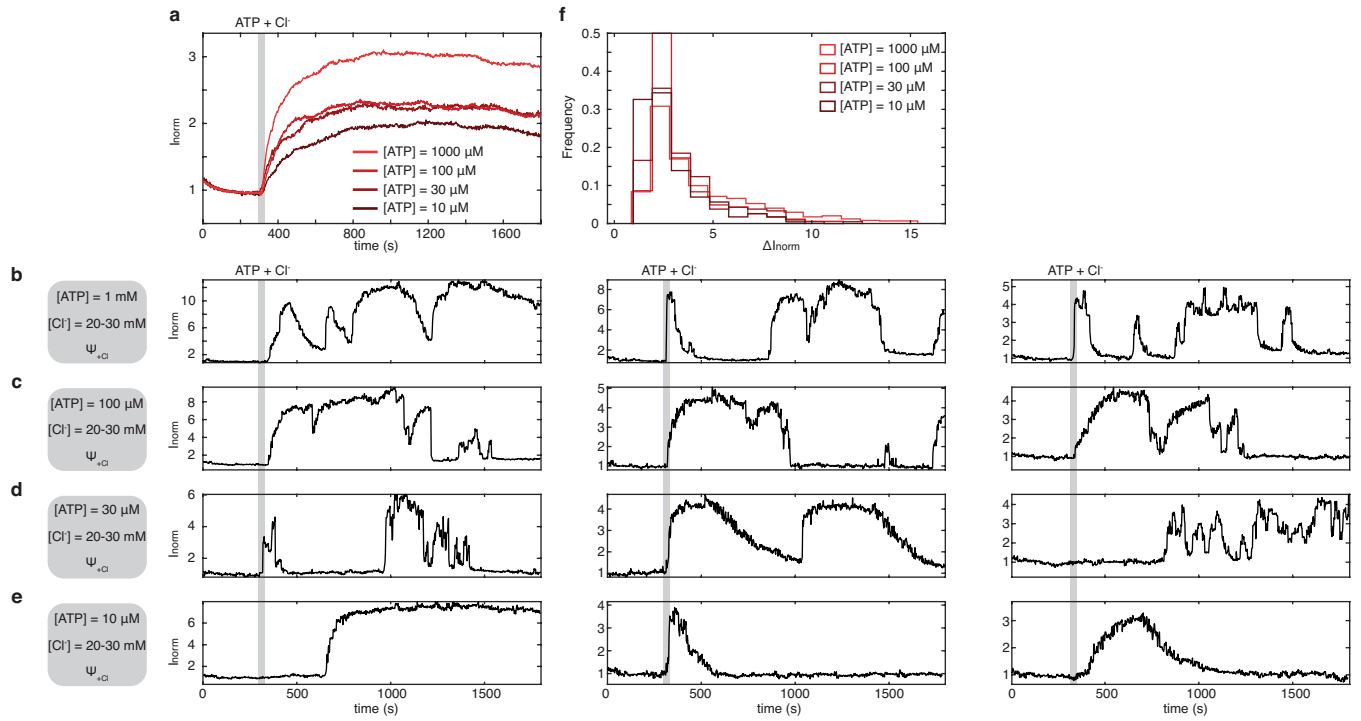
Extended Data Fig. 5 | ~30% of mode-switching events are too fast to reach a pH plateau or decay to zero ΔpH . In approximately 30% of single-molecule data, dynamics of switching are faster than the dynamics of pumping or leakage. **a**, Schematic representation of different cases of mode-switching events, pH build-up and leakage lifetimes. Top left: the pumping dwell time (t_{on}) is longer than the pH build-up time ($\tau_{\text{build-up}}$), allowing for the acidification to reach a constant plateau (ΔpH_{\max}). Bottom left: t_{on} is shorter than $\tau_{\text{build-up}}$, and therefore ΔpH_{\max} cannot be reached. Top right: the inactive dwell time (t_{off}) is longer than the leakage lifetime (τ_{leak}) allowing for the ΔpH to reach zero. Bottom right: t_{off} is shorter than τ_{leak} and therefore the pH will not be able to reach the baseline value. **b**, Populations of pH build-up lifetimes and proton-pumping mode dwell durations. pH build-up data (red) was produced by fitting single exponentials on kinetic traces during periods of rise of activity. Data for t_{on} (yellow) is taken from Fig. S6b, second row and shown in a logarithmic scale. **c**, Populations of leakage lifetimes of periods of activity of SV_h and resting dwell times. Dataset for leakage is the same as that in Fig. 2e while dataset for resting dwells is taken from Fig. S6c, second row.

Article



Extended Data Fig. 6 | Electrochemical regulation of mode-switching

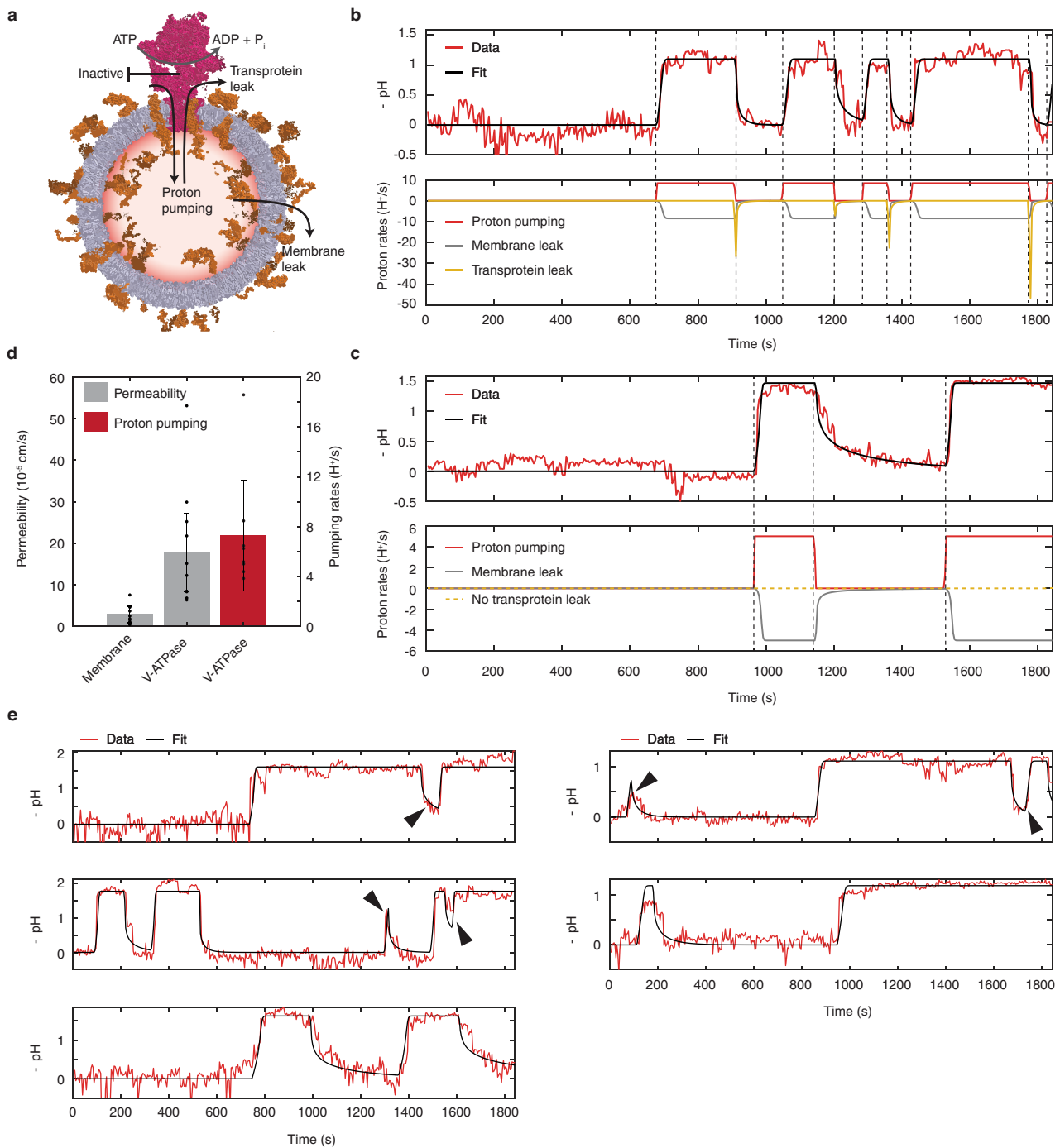
dynamics. **a**, Proton-pumping mode probabilities in the presence or absence of chloride. No statistical significance was detected between the two populations. Error bars correspond to one s.d. between experiments, $n=8$ (red) and $n=5$ (grey) for $\Delta\Psi_{+Cl}$ and $\Delta\Psi_{-Cl}$ respectively. A two-tailed Mann-Whitney U test gave a P-value = 0.62 (n.s.). **b**, Representation of the free energy landscape for the two different electrochemical conditions. The forward activation barriers, $\Delta G_{on}^{+Cl} = 86.2 \text{ kJ} \cdot \text{mol}^{-1} \pm 0.3 \text{ kJ} \cdot \text{mol}^{-1}$ and $\Delta G_{on}^{-Cl} = 86.7 \text{ kJ} \cdot \text{mol}^{-1} \pm 0.4 \text{ kJ} \cdot \text{mol}^{-1}$, are higher than those for backwards activation, $\Delta G_{off}^{+Cl} = 85.3 \text{ kJ} \cdot \text{mol}^{-1} \text{kJ} \cdot \text{mol}^{-1} \pm 0.6 \text{ kJ} \cdot \text{mol}^{-1}$ and $\Delta G_{off}^{-Cl} = 86.3 \text{ kJ} \cdot \text{mol}^{-1} \pm 1.3 \text{ kJ} \cdot \text{mol}^{-1}$, highlighting the fact that the probability the V-ATPase is found in a proton-pumping mode is higher. Additionally, both forward and backwards activation barriers were lower when the membrane potential was released which indicates that the frequency of transitions between modes is higher.



Extended Data Fig. 7 | Acidification kinetics under different catalytic substrate concentrations. Data analyzed from these experiments was used for calculating pumping-mode probabilities (Fig. 4d) and dwell times (Extended Data Fig. 6). **a**, Ensemble average acidification kinetics of SV_h at different concentrations of ATP. Activity was initiated upon addition of ATP

and 20-30 mM chloride. **b–e**, Typical single molecule traces at different concentrations of ATP (as stated in corresponding grey boxes). **f**, Histograms of maximum intensity of single molecule data. Total number of experiments was $n = 4-8$.

Article



Extended Data Fig. 8 | Non-equilibrium physical modelling of pumping, resting and leaky modes provides the single-molecule pumping and leaking rate. **a**, Schematic illustration of the main parameters used in the model. Note: this illustration is also shown in Fig. 2a. **b,c**, Top: Representative single-molecule traces displaying mode-switching dynamics. Proton pumping was stochastically interrupted by inactive and proton-leaky modes. During active periods of the V-ATPase, a dynamic equilibrium between proton-pumping and passive leakage is established, therefore reaching a single acidification plateau. Leakage currents are a convolution of transprotein and passive membrane proton efflux. Transprotein leakage currents are temporally distinct from proton pumping and may activate directly after the enzyme switched off. Data was fitted with a non-equilibrium model as described in the supplementary information. Pumping rates and permeabilities (both membrane and transprotein) are calculated as free parameters by the model. Bottom:

Pumping dynamics for the proton-pumping rate (red), the passive membrane efflux rate (grey) and the transprotein efflux rate (yellow). In b the transprotein leak was the primary efflux pathway while in c proton efflux manifested only passively through the membrane. **d**, Proton pumping rates and permeability estimates of the model for the data shown in this figure (b, c, and e). Pumping rates were found to be $7 \pm 5 H^+/s$. Membrane and V-ATPase permeability were $3 \pm 2 \times 10^{-5} \text{ cm/s}$ and $18 \pm 9 \times 10^{-5} \text{ cm/s}$. Transprotein permeability of the V-ATPase is nearly an order of magnitude larger than passive membrane permeability indicating the regulatory importance of the proton-leaky mode. Error bars correspond to one s.d. Number of independent model outputs are $N = 8, 11$ and 8 for membrane permeability, V-ATPase permeability and proton-pumping rates respectively. **e**, Additional single-molecule traces fitted the model. Arrows point out the mode-switching events during which dynamic ($\Delta pH = \Delta pH_{\max}$) or static (baseline, $\Delta pH = 0$) equilibrium was not reached.

Reporting Summary

Nature Portfolio wishes to improve the reproducibility of the work that we publish. This form provides structure for consistency and transparency in reporting. For further information on Nature Portfolio policies, see our [Editorial Policies](#) and the [Editorial Policy Checklist](#).

Statistics

For all statistical analyses, confirm that the following items are present in the figure legend, table legend, main text, or Methods section.

n/a Confirmed

- The exact sample size (n) for each experimental group/condition, given as a discrete number and unit of measurement
- A statement on whether measurements were taken from distinct samples or whether the same sample was measured repeatedly
- The statistical test(s) used AND whether they are one- or two-sided
Only common tests should be described solely by name; describe more complex techniques in the Methods section.
- A description of all covariates tested
- A description of any assumptions or corrections, such as tests of normality and adjustment for multiple comparisons
- A full description of the statistical parameters including central tendency (e.g. means) or other basic estimates (e.g. regression coefficient) AND variation (e.g. standard deviation) or associated estimates of uncertainty (e.g. confidence intervals)
- For null hypothesis testing, the test statistic (e.g. F , t , r) with confidence intervals, effect sizes, degrees of freedom and P value noted
Give P values as exact values whenever suitable.
- For Bayesian analysis, information on the choice of priors and Markov chain Monte Carlo settings
- For hierarchical and complex designs, identification of the appropriate level for tests and full reporting of outcomes
- Estimates of effect sizes (e.g. Cohen's d , Pearson's r), indicating how they were calculated

Our web collection on [statistics for biologists](#) contains articles on many of the points above.

Software and code

Policy information about [availability of computer code](#)

Data collection

Microscopy data was collected using the commercially available software:

- xcellence rt (version 2.0, Olympus, now discontinued)
- cellSens Dimension (version 3.2, Olympus)

Data analysis

All data analysis and modelling was performed in custom software written in MATLAB 2018a and newer versions up to 2020b. Bayesian filtering algorithm was written in C++11.

For manuscripts utilizing custom algorithms or software that are central to the research but not yet described in published literature, software must be made available to editors and reviewers. We strongly encourage code deposition in a community repository (e.g. GitHub). See the Nature Portfolio [guidelines for submitting code & software](#) for further information.

Data

Policy information about [availability of data](#)

All manuscripts must include a [data availability statement](#). This statement should provide the following information, where applicable:

- Accession codes, unique identifiers, or web links for publicly available datasets
- A description of any restrictions on data availability
- For clinical datasets or third party data, please ensure that the statement adheres to our [policy](#)

The data that support the findings of this study are available from the corresponding authors upon request.

Human research participants

Policy information about [studies involving human research participants and Sex and Gender in Research](#).

Reporting on sex and gender	<input type="checkbox"/> Not applicable
Population characteristics	<input type="checkbox"/> Not applicable
Recruitment	<input type="checkbox"/> Not applicable
Ethics oversight	<input type="checkbox"/> Not applicable

Note that full information on the approval of the study protocol must also be provided in the manuscript.

Field-specific reporting

Please select the one below that is the best fit for your research. If you are not sure, read the appropriate sections before making your selection.

Life sciences Behavioural & social sciences Ecological, evolutionary & environmental sciences

For a reference copy of the document with all sections, see nature.com/documents/nr-reporting-summary-flat.pdf

Life sciences study design

All studies must disclose on these points even when the disclosure is negative.

Sample size	All sample sizes used in the present manuscript are n>=3 with the only exception of data shown in Figure S7 where n = 2. n is defined as the number of independent runs of recordings per condition. More specifically each independent experiment included a freshly thawed aliquot and a new microfluidic flow chamber was used. The sample for each independent experimental run contained a total of approximately 1000 liposomes in each FOV per repeat as stated in the manuscript. Liposomes were detected via a particle tracking algorithm and selected via various thresholding techniques. Due to each experimental run containing ~1000 we could extract large number for reliable statistical analysis.
Data exclusions	Single vesicle data were identified via single particle detection algorithms. SNR thresholding was used to separate active vesicles. Step-counting on single-vesicle traces was used to determine the number of molecules per vesicle. Single molecule data used for dwell time analysis was used only if stochastic behavior was observed. Details on data exclusion can be found in the manuscript.
Replication	Reproducibility was reliably verified by performing experiments on separate days on frozen and aliquoted samples and freshly made buffers. All data included has been replicated. Data was replicated by up to 15 independent experiments (typically n = 3-15). Only exception is the data in Fig. S7 (n = 2) and the cryo-electron micrographs in Fig. S1 and S2 (n = 1, multiple micrographs).
Randomization	Randomization is not applicable. Single-molecule data is intrinsically randomized as their properties are unknown prior to investigation.
Blinding	Blinding is not applicable. No a priori knowledge was and could be assumed prior to the investigation of the switching dynamics of the V-ATPase. All data analyzed via sets of strict rules and/or automated processes as discussed in the manuscript.

Reporting for specific materials, systems and methods

We require information from authors about some types of materials, experimental systems and methods used in many studies. Here, indicate whether each material, system or method listed is relevant to your study. If you are not sure if a list item applies to your research, read the appropriate section before selecting a response.

Materials & experimental systems		Methods	
n/a	Involved in the study	n/a	Involved in the study
<input checked="" type="checkbox"/>	<input type="checkbox"/> Antibodies	<input checked="" type="checkbox"/>	<input type="checkbox"/> ChIP-seq
<input checked="" type="checkbox"/>	<input type="checkbox"/> Eukaryotic cell lines	<input checked="" type="checkbox"/>	<input type="checkbox"/> Flow cytometry
<input checked="" type="checkbox"/>	<input type="checkbox"/> Palaeontology and archaeology	<input checked="" type="checkbox"/>	<input type="checkbox"/> MRI-based neuroimaging
<input type="checkbox"/>	<input checked="" type="checkbox"/> Animals and other organisms		
<input checked="" type="checkbox"/>	<input type="checkbox"/> Clinical data		
<input checked="" type="checkbox"/>	<input type="checkbox"/> Dual use research of concern		

Animals and other research organisms

Policy information about [studies involving animals](#); [ARRIVE guidelines](#) recommended for reporting animal research, and [Sex and Gender in Research](#)

Laboratory animals	Adult Wistar rats were purchased from Charles River Laboratories, or Janvier, and were kept until 5 to 6 weeks of age at a 12:12 hr light/dark cycle with food and water ad libitum.
Wild animals	The study did not involve wild animals.
Reporting on sex	Not applicable. The molecular function of the V-ATPase in synaptic vesicles, which was analysed in this study, is not affected by sex.
Field-collected samples	The study did not contain samples collected from the field.
Ethics oversight	Certificate of approval for using animals was issued by the Landkreis Goettingen Office of Veterinary Affairs and Consumer Protection. Extraction of brain material from animals does not require an ethics committee oversight according to the law issued by the state of Lower Saxony. The state itself in this case should act as the ethics committee.

Note that full information on the approval of the study protocol must also be provided in the manuscript.